The Genesis of the Giant Shuangjianzishan Epithermal Ag-Pb-Zn Deposit, Inner Mongolia, Northeastern China

Degao Zhai[1, 2*], Anthony E. Williams-Jones[2], Jiajun Liu[1], David Selby[3, 4], Panagiotis C. Voudouris[5], Stylianos Tombros[6], Kuan Li[1], Peilin Li[1], Hongjun Sun[7]

[1]*State Key Laboratory of Geological Processes and Mineral Resources, School of Earth Sciences and Resources, China University of Geosciences, Beijing, 100083, China*

[2]*Department of Earth and Planetary Sciences, McGill University, Quebec, 3450, Canada*

[3]*Department of Earth Sciences, Durham University, Durham, DH1 3LE, UK*

[4]*State Key Laboratory of Geological Processes and Mineral Resources, School of Earth Resources, China University of Geosciences, Wuhan, 430074, China*

[5]*Department of Mineralogy-Petrology, National and Kapodistrian University of Athens, 15784, Athens, Greece*

[6]*Department of Geology, University of Patras, Rion, 26500, Greece*

[7]*Tiantong Mining Company, Chifeng, 024000, China*

[*]E-mail: *dgzhai@cugb.edu.cn*

Revised submission to: *Economic Geology*

With 15 Figures and 5 Tables

21-July-2019

Abstract

The newly-discovered Shuangjianzishan Ag-Pb-Zn deposit with 145 Mt of ore grading 128.5 g/t Ag (locally up to 32,000 g/t) and 2.2 wt.% Pb+Zn is located in the Great Hinggan Range (GHR) Metallogenic Belt, northeastern China, and is currently the largest Ag deposit in Asia. The Ag-Pb-Zn orebodies occur as veins and are hosted primarily by a Permian slate. Recent drilling and core logging have identified a partially Mo-mineralized granite porphyry intrusion adjacent to the Ag-Pb-Zn mineralized veins. This well-preserved magmatic-hydrothermal system therefore offers an excellent opportunity to evaluate the possible temporal and genetic relationship between Mo-mineralized porphyry intrusions and Ag-Pb-Zn veins. Three primary paragenetic stages of veining have been recognized: (I) early pyrite+quartz±K-feldspar, (II) main ore sulfide+sulfosalt+quartz+calcite+sericite+chlorite±epidote, and (III) post-ore quartz. The silver mineralization occurs mainly in the late paragenetic part of Stage II, in which canfieldite (Ag_8SnS_6), argentite (Ag_2S) and freibergite [$(Ag, Cu)_{12}Sb_4S_{13}$] are the dominant Ag-bearing ore minerals. A combination of ore mineral chemical and sulfur isotope geothermometers and physicochemical calculations suggest that the Ag-Pb-Zn mineralization took place at a temperature of 250° to 200°C, a pH of 6.7 to 5.6, and a $\Delta \log fO_2$ (HM) of -2.4 to -8.7.

A conspicuous enrichment of Sn and Se in the ore, which is represented by minerals containing the metal suite Ag-Pb-Zn-(Cu-Sn-Se-Sb), likely reflects a close genetic association between the base metal mineralization and a magma. In situ analyses show that the $\delta^{34}S$ values of the sulfides and Ag-bearing sulfosalts from the Ag-Pb-Zn mineralized veins vary from -4.67 to +2.44‰; the mean value is -2.11 ± 1.49‰ (n=77). The calculated mean $\delta^{34}S_{H2S}$ value of the ore-forming fluid is -1.65 ± 0.83‰, which is indicative of a magmatic sulfur source. In situ Pb isotope analyses of the ore minerals yielded a narrow range of values ($^{206}Pb/^{204}Pb$ of 18.243 to 18.310, $^{207}Pb/^{204}Pb$ of 15.503 to 15.563 and $^{208}Pb/^{204}Pb$ of 38.053 to 38.203, n=59). Comparisons to corresponding isotopic data for the various rock units in the area and sulfides from nearby ore deposits indicate that there were substantial contributions of Pb, and other metals (e.g., Ag and Zn), to the Shuangjianzishan deposit from a Mesozoic granitic source.

Diorite-granodiorite dikes and dacite are crosscut by the Ag-Pb-Zn veins, and therefore, pre-date ore formation. These rock units have zircon U-Pb ages of 250.2 ± 2.0 and 133.9 ± 1.4 Ma, respectively. A concealed, weakly Mo-mineralized granite porphyry intrusion proximal to the Ag-Pb-Zn mineralized vein system yielded zircon U-Pb ages of 134.4 ± 1.0 (MSWD = 0.1) and 134.4 ± 1.0 Ma (MSWD = 0.2), for coarse- and fine-grained facies, respectively. These ages are indistinguishable within the uncertainty

from the zircon ages for the dacite and a granite intrusion ~2 km north of the mineralized veins, which has a weighted mean zircon U-Pb age of 135.2 ± 1.4 Ma (MSWD = 0.78). Molybdenite from three quartz vein/veinlet samples hosted by slate immediately above the porphyry intrusion yielded Re-Os model ages from 136.3 ± 0.9 to 133.7 ± 1.2 Ma and a weighted mean Re-Os age of 134.9 ± 3.4 Ma. Finally, three pyrite samples separated from the Ag-Pb-Zn mineralized veins have a weighted mean Re-Os model age of 135.0 ± 0.6 Ma. The very similar zircon U-Pb ages for the Mo mineralized granite porphyry and dacite, and Re-Os ages for molybdenite and pyrite in the Shuangjianzishan ore district indicate that the Mesozoic magmatic-hydrothermal activity was restricted to a relatively short time interval (~136 to 133 Ma). They also suggest that the weakly Mo-mineralized granite porphyry was likely the source of the fluids and metals that produced the Ag-Pb-Zn mineralization.

Based on our geological observations and an extensive analytical database, a model is proposed for the genesis of the giant Shuangjianzishan Ag-Pb-Zn deposit in which the ore-forming fluid and its metals (i.e., Ag, Pb, and Zn) were exsolved during crystallization of the final phase of a composite granite porphyry intrusion. This fluid transported metals to the distal parts of the system, where they were deposited in pre-existing faults or fractures created by the withdrawal of magma during the waning stages of the magmatic-hydrothermal event. The present study of the Shuangjianzishan Ag-Pb-Zn deposit and those of other magmatic-hydrothermal ore deposits in the region provide compelling evidence that the widespread Mesozoic felsic magmatism and Ag-Pb-Zn mineralization in the southern GHR took place in an intracontinental extensional tectonic setting, which was synchronous with, and spatially associated to, Paleo-Pacific slab rollback and lithospheric delamination and thinning.

Introduction

Silver-lead-zinc vein-type mineralization has made a major contribution to the global supply of Ag and base metals. In addition, its close temporal, spatial and genetic association with porphyry-type mineralization has been long recognized and is well documented (e.g., Guilbert and Park, 1986; Einaudi et al., 2003; Sillitoe, 2010; Catchpole et al., 2015). Many studies of magmatic-hydrothermal systems have developed genetic models for porphyry ore systems (Einaudi et al., 2003; Heinrich, 2005; Williams-Jones and Heinrich, 2005; Seedorff et al., 2005; Rusk et al., 2008; Sillitoe, 2010; Richards, 2011; Wilkinson, 2013; Chiaradia, 2014). In contrast, much less attention has been paid to the Ag-Pb-Zn vein

mineralization, which typically occurs peripheral to, adjacent to, or is superimposed on the mineralized porphyry systems (Seedorff et al., 2005; Sillitoe, 2010; Zhai et al., 2017; Rottier et al., 2018a). The close spatial-temporal relationship between porphyry Cu-Mo and Ag-Pb-Zn vein mineralization has provided a very useful guide for exploration that has led to the discovery of new Ag-Pb-Zn veins adjacent to porphyry Cu-Mo deposits and vice versa, e.g., the Butte ore district (Rusk et al., 2008). Some Ag-Pb-Zn vein deposits, however, do not appear to be genetically linked to porphyry intrusions and their genesis still remains controversial (Beaudoin and Sangster, 1992; Kissin and Mango, 2014).

Characteristic features of Ag-Pb-Zn vein-type deposits can be summarized as follows: (1) a common metal suite of Ag-Pb-Zn-(±Cu±Au±Bi±Sb±As), (2) a sulfide-rich ore (commonly massive) composed of galena, sphalerite and a variety of Ag-bearing sulfosalts and a gangue of quartz and calcite, (3) the occurrence of the orebodies as epigenetic open-space filled veins spatially associated with sericitization and silicification, (4) in some cases, a well-developed metal and alteration zonation at the deposit scale, (5) deposition mostly under epithermal conditions from magmatic-hydrothermal fluids of low to moderate salinity (commonly <10 wt.% NaCl equivalent), and (6) structural control of the mineralization by late regional faults (e.g., Einaudi, 1981; Baumgartner et al., 2009; Bendezú and Fontboté, 2009; Fontboté and Bendezú, 2009; Kissin and Mango, 2014; Catchpole et al., 2015; Rottier et al., 2018a, b; Zhai et al., 2019a, and references therein). These polymetallic vein deposits, which historically have been an important source of Zn, Pb, and Ag in the North American Cordillera and in Peru, are also referred to as Cordilleran base metal deposits, Butte-type vein deposits, polymetallic veins, or zoned base metal veins (e.g., Einaudi, 1981; Guilbert and Park, 1986; Einaudi et al., 2003; Bendezú and Fontboté, 2002, 2009; Baumgartner et al., 2009; Fontboté and Bendezú, 2009; Catchpole et al., 2015; Rottier et al., 2016, and references therein).

The Great Hinggan Range (GHR) Metallogenic Belt, NE China, hosts a number of porphyry Mo-(Cu), skarn Fe-(Sn), epithermal Au-Ag, and Ag-Pb-Zn vein deposits (e.g., Zeng et al., 2011; Ouyang et al., 2014; Mao et al., 2014; Zhai et al., 2014a, b, 2018a, 2019b; Shu et al., 2016; Chen, Y., et al., 2017). In particular, it contains more than 30 Ag-Pb-Zn ore deposits with total resources of >57,000 t of silver (Zhai et al., 2017), making it the largest silver province in China. The Ag-Pb-Zn vein-type deposits are particularly common in the southern segment of the GHR, where recent discoveries include the Shuangjianzishan, Bianjiadayuan, Bairendaba, and Weilasituo deposits (e.g., Ouyang et al., 2014; Liu, C., et al., 2016; Liu, Y., et al., 2016; Zhai et al., 2017). Among them, the largest is the Shuangjianzishan deposit with reserves

exceeding 145 Mt of ore at an average grade of 128.5 g/t Ag (≈ 18,630 tons Ag) and 2.2 wt.% Pb+Zn (Kuang et al., 2014), making this deposit the largest Ag deposit in Asia. It also has an extremely high Ag grade, which locally exceeds 32,000 g/t.

Recently, a concealed, weakly Mo-mineralized granite porphyry intrusion was intersected in drill holes adjacent to the Shuangjianzishan Ag-Pb-Zn veins. Whether-or-not the Ag-Pb-Zn vein mineralization is related to this newly-discovered porphyry intrusion has been unclear, and resolving this issue is important for exploration in the area. Several studies of the Shuangjianzishan deposit, mostly published in Chinese or reported in student dissertations, have addressed the ore deposit geology (Kuang et al., 2014), mineralogy (Wu et al., 2014; Zhai et al., 2019c), whole rock geochemistry (Liu, C., et al., 2016; Gu et al., 2017), magmatic rock and ore geochronology (Wu et al., 2013; Wang et al., 2016; Ouyang et al., 2016; Liu, C., et al., 2016; Wang, F., 2017; Zhang, 2018), and S-Pb isotope geochemistry (Wang, 2015; Jiang, B., et al., 2017; Wang, X., 2017). However, questions related to the sulfur and metal source, the timing of mineralization, and the genesis of the deposit remain unresolved and greatly debated. For example, there is no consensus on the age of ore formation. Wu et al. (2013) proposed a mineralization age of 132.7 ± 3.9 Ma using the sphalerite Rb-Sr method, whereas Wang et al. (2016) obtained ages for alteration and mineralization of 146.9 ± 1.9 and 162.6 ± 2.6 Ma using sericite Ar-Ar and molybdenite Re-Os methods, respectively. Wang, F. (2017) subsequently obtained an age of 159 ± 6 Ma by applying the Re-Os method to arsenopyrite and pyrite, and 148 ± 1 Ma using the U-Pb method (hydrothermal zircon). Finally, Gu et al. (2017) obtained a zircon U-Pb age for the Mo-mineralized granite porphyry of 133.4 ± 1.2 Ma, which they proposed was associated with the Ag-Pb-Zn mineralization.

In this contribution, we present the results of a comprehensive investigation of the Shuangjianzishan Ag-Pb-Zn deposit, utilizing ore mineralogical, textural, petrochemical, sulfide Re-Os and zircon U-Pb geochronological, and in situ S and Pb isotopic data. Our new data are used to constrain the source and nature of the hydrothermal fluid, the metal source, and the timing of ore mineral deposition, and to determine its genetic relationship to the porphyry intrusion. The results of this study show that the Ag-Pb-Zn veins are part of a magmatic-hydrothermal system related to a nearby Mo-mineralized granite porphyry and reflect the relatively high solubility of the metals (e.g., Ag, Pb, and Zn), which facilitated their transport to the distal parts of the system, where they were deposited in pre-existing faults or fractures created by magma withdrawal during the waning stages of magmatic-hydrothermal activity.

Regional Geology

The Shuangjianzishan Ag-Pb-Zn deposit is located in the Great Hinggan Range (GHR) Metallogenic Belt, which lies in the easternmost segment of the Central Asian Orogenic Belt (CAOB) (Fig. 1A). The CAOB evolved through complex closure of the Paleo-Asian Ocean from the Neoproterozoic to the late Permian (Wilde, 2015), which separated the Siberian craton in the north from the Tarim and North China cratons in the south (Fig. 1A). It formed via successive accretion of arc complexes, accompanied by the emplacement of immense volumes of granitic magma (Jahn et al., 2000), and is believed to have been the world's largest site of juvenile crust formation in the Phanerozoic era (Jahn, 2004). This region records complex processes involving tectonic events that marked the transition in the late Permian-Early Triassic from the dominantly NE-SW directed motion of the Paleo-Asian plate to the E-W directed motion of the Paleo-Pacific plate (e.g., Li, 2006; Wilde, 2015; Zhou et al., 2018, and references therein).

The tectonic evolution of the CAOB since the late Permian can be summarized briefly as follows: (i) closure of the Paleo-Asian Ocean was completed in the late Permian (~260 Ma); (ii) a switch in geodynamic setting took place in the late Permian-Early Triassic (~260-250 Ma) that is reflected by the Paleo-Asian Ocean closure and the onset of tectonism associated with subduction of the Paleo-Pacific plate; (iii) events associated with the westward advance of the Paleo-Pacific plate in the Early Jurassic-early Cretaceous (~250-140 Ma); and (iv) the slab rollback of the Paleo-Pacific plate after the early Cretaceous (~140 Ma), which created an extensional setting associated with thinning and delamination of the lithosphere (e.g., Li, 2006; Wang et al., 2006; Zhang et al., 2010; Wu et al., 2011; Wilde, 2015; Liu, K., et al., 2017; Zhou et al., 2018, and references therein). The region underwent widespread Mesozoic volcanic and intrusive activity (Fig. 1B), including emplacement of I- and A-type granitoids at different stages (i.e., Early to Late Triassic and late Jurassic to early Cretaceous) of the geotectonic evolution (Xiao et al., 2004; Wu et al., 2005, 2011), which today underlie >50% of the surface area in the mountainous regions (HBGMR, 1993). Compared with other areas in the CAOB, NE China was strongly affected by Paleo-Pacific subduction and, as a result, is one of the most metallogenically important areas of the eastern Asian Mesozoic continental margin (Wu et al., 2011).

The southern segment of the GHR Metallogenic Belt hosts numerous porphyry Mo-(Cu), skarn Fe-(Sn), and Ag-Pb-Zn vein deposits (Fig. 1C; Ouyang et al., 2014; Shu et al., 2016; Chen, Y., et al., 2017; Gao et al., 2018; Zhai et al., 2018b). These deposits are hosted mainly by Permian strata and Mesozoic granites (Fig. 1C), the latter of which were produced during regional Mesozoic magmatism (Mao et al.,

2014; Ouyang et al., 2015; Shu et al., 2016; Zhai et al., 2017; Chen, Y., et al., 2017; Gao et al., 2018, and references therein). Recent exploration has revealed that Ag-Pb-Zn vein deposits are very common in the region (Fig. 1C), as shown by discovery of the Shuangjianzishan, Bianjiadayuan, Bairendaba and Weilasituo deposits (e.g., Ouyang et al., 2014; Liu, Y., et al., 2016; Wang et al., 2017; Zhai et al., 2018c), which define the southern segment of the GHR that is the most important Ag-Pb-Zn metallogenic belt in northern China.

Available geochronological data indicate that magmatic-hydrothermal deposits in this area formed during two distinct metallogenic events, namely, an early event in the Permian and Triassic (~290 to 230 Ma; Wan et al., 2009; Zhou et al., 2014; Duan et al., 2015; Jiang, S., et al., 2017) and a late event in the Jurassic and Cretaceous (~160 to 130 Ma; Zeng et al., 2015; Ouyang et al., 2015; Liu, Y., et al., 2016; Wang et al., 2017; Jiang, S., et al., 2017). Numerous age determinations of porphyry Mo-(Cu) and skarn Fe-(Sn) deposits suggest that the magmatic-hydrothermal systems developed mainly during the second metallogenic event (Fig. 1C), synchronously with granite emplacement (Mao et al., 2014; Ouyang et al., 2015; Shu et al., 2016; Zhai et al., 2017; Gao et al., 2018). However, reliable ages for the vein-type Ag-Pb-Zn mineralization are generally lacking, mostly because these deposits have received much less study, and more importantly, because of the paucity of minerals that can be easily and accurately dated. However, the ages of some of these deposits have been estimated reliably where it has been possible to establish a close genetic association between the porphyry and polymetallic vein-type mineralization (e.g., the Bianjiadayuan and Weilasituo deposits; Zhai et al., 2017; Wang et al., 2017).

Ore Deposit Geology

The main rock-types exposed in the Shuangjianzishan ore district are late Permian slates, Mesozoic volcanic rocks and Quaternary gravel (Fig. 2A). The Permian slates are part of the Dashizhai Formation, and form >30% of the surface outcrop in the mine area (Fig. 2A). The slates are >950m thick, and generally strike NE and dip NW at 55-65°. They are the main host to the ores (Fig. 2A, B). The volcanic rocks are located mainly to the southeast of the Ag-Pb-Zn mineralized zones, unconformably overlie the slates (Fig. 2A) and are interpreted to have been emplaced in the Jurassic (Wu et al., 2014). They belong mainly to the Xinmin Formation, and consist largely of dacite lava and rhyolitic tuff with a thickness of >200 m; some of the Ag-Pb-Zn mineralized veins crosscut these rock units (Fig. 2A). Quaternary gravels, which consist of unsorted rock fragments and are 15 to 50 m thick, cover much of the district (Fig. 2A).

The only exposed intrusive rock in the district is a granitic pluton located ~2 km to the north of the Shuangjianzishan ore deposit (Fig. 2A). An unexposed granite porphyry intrusion was intersected in the core of drill hole ZK12-37 from a depth of 516 m to the bottom of the hole at 1080 m. This intrusion is located approximately 800 m to the northwest of the main mineralized veins (Fig. 2A). Texturally, the porphyry has been subdivided into a lower coarse-grained facies and an upper fine-grained facies that intrudes the coarse-grained facies and is observed to a depth of 846 m (Fig. 3A). The fine-grained facies shows evidence of having undergone strong potassic and silicic alteration, and contains numerous quartz-molybdenite veins (0.1 to 2 cm width). Numerous K-feldspar-quartz veinlets/stockworks and less abundant magmatic-hydrothermal breccias cemented by minor Mo mineralization also occur in the fine-grained porphyry (Fig. 3A). In contrast, the coarse-grained facies is only altered near its contact with the fine-grained facies and is unaltered at depth and free of quartz-molybdenite veins. The overlying slates have been sericitized and silicified for ~150 m above the fine-grained porphyry and locally contain molybdenite-quartz ± albite veins/veinlets and zones of hydrothermal brecciation (Fig. 3A). On the basis of the above observations, we speculate that the fine-grained porphyry may be genetically related to the Ag-Pb-Zn mineralization considered in this paper. In addition to the granitic pluton and granite porphyry, there are diorite and granodiorite dikes that strike NW or NE, dip ~60° to the SE, vary in width from 1 to 8 m, and have been traced along strike for distances of 50 to 300 m. Several of these dikes are crosscut by the Ag-Pb-Zn mineralized veins (Figs. 2A and 3B), indicating that they were intruded prior to the mineralization.

The major faults in the district have NW-, NE- and NS-strikes. However, most Shuangjianzishan Ag-Pb-Zn veins were emplaced parallel to a NW-striking fault zone (Fig. 2A). This fault zone varies in width from 500 to 800 m, strikes 300-310°, dips NE at 55 to 65° and has been traced for a distance of > 5000 m. These faults are characterized by extensional shear features. A few veins were emplaced in a NE-striking fault zone (Fig. 2A), which strikes 30-50° and dips SE at ~60°. Minor veins are also hosted by the NS-striking fault zones (Fig. 2A). The NW- and NE-striking faults are observed to have been truncated by some of the Ag-Pb-Zn-barren NS-striking faults.

The Shuangjianzishan Ag-Pb-Zn deposit was discovered in 2013 and has been mined since that time. More than 70 major veins and numerous stockworks and disseminations have been identified, all of which are hosted by the Permian slate. According to a 2018 exploration report (Zhang, 2018), the deposit has a total resource of 145 Mt of ore containing >18.6 Kt of Ag with an average grade of 128.5

g/t, 0.87 Mt of Pb with an average grade of 0.6 wt.% and 2.32 Mt of Zn with an average grade of 1.6 wt.%. This makes Shuangjianzishan the largest Ag deposit in Asia (Kuang et al., 2014). Two separate ore zones 4.7 km apart, namely Shuangjianzishan in the west and Xinglongshan in the east, have been identified (Kuang et al., 2014). The bulk of the economic mineralization, however, is in the eastern ore zone (Fig. 2A). Although several oxidized veins are exposed in slate outcrops (Fig. 4A), most of the mineralized veins are not exposed (Fig. 4B-D). Mineralized veins fill fractures that strike ~310° and dip SW at 50-60°, whereas they are sparse in the NE- and NS-striking fault zones. The orebodies comprise sets of parallel veins concentrated in zones ranging from 2 to 10 m in width, although locally these zones range up to 30 m in width; individual veins range up to 10 m in width (Fig. 4B, C). They (the orebodies) generally have strike lengths between 100 and 800 m, and extend vertically ~500 m (Fig. 2B). Stockwork veins and disseminated mineralization have been discovered adjacent to the major veins (Fig. 4B) or in structural domains associated with faults having orientations different from those controlling the major veins.

Hydrothermal alteration is intense around the major Ag-Pb-Zn mineralized veins, and is characterized by an assemblage of sericite, chlorite, quartz, and calcite. This alteration is concentrated in halos that are distributed symmetrically on the two sides of the mineralized veins (Fig. 4B, C). In addition, the slates have experienced silicification and subordinate weaker potassic alteration (secondary K-feldspar), which predated the main sulfide mineralization. This alteration is associated with euhedral pyrite, or locally pyrite-quartz veins. The latter are consistently cut by the main mineralized veins (Fig. 4D). The alteration associated with the Ag-Pb-Zn veins (Fig. 4D-G) includes a sub-assemblage of quartz-sericite ± chlorite that was closely related to Ag mineral deposition (Fig. 4E), particularly the very high grade and massive ores (Fig. 4E, F). The final stage of alteration is represented by quartz, which occurs as narrow veins (1-5 mm width) cutting the Ag-Pb-Zn mineralized veins (Fig. 4D).

Sampling and analytical methods

Ore mineral textures and compositions

More than ninety samples were collected from different mining levels and drill holes from the Shuangjianzishan deposit and more than 120 polished thin sections were examined in reflected and transmitted light. A Zeiss Supra 55 Sapphire field emission scanning electron microscope (FESEM) coupled with an Oxford energy-dispersive X-ray spectrometer (EDS), located at the China University of Geosciences Beijing (CUGB), was used to identify the minerals by determining their compositions semi-

quantitatively and imaging textural relationships among them. Element line scanning was undertaken for Ag Lα, Sb Lα, Pb Mα, Fe Kα, Cu Kα, Se Kα, and S Kα using an accelerating voltage of 20 kV and a working distance of 15 mm. An in-lens detector for secondary electron imaging was used to characterize topographic features, and an AsB detector was used to visualize compositional differences among the minerals (backscattered electron images). Samples were coated with an ~10 nm thick platinum film for electric conduction before analysis.

The compositions of the sulfides and sulfosalts were determined using a JEOL 8230 Superprobe equipped with wavelength- and energy-dispersive X-ray detectors and a back-scatter electron detector at the Microprobe Center, Chinese Academy of Geological Sciences (CAGS). The accelerating voltage was 20 kV. The beam current and counting times for the major elements were 20 nA and 20 s, respectively (10 s for background measurement), and the beam diameter was 1 μm. Natural and synthetic mineral standards of chalcopyrite, sphalerite, galena, pyrrhotite, InAs and native Ag, Sb, Se, Sn were utilized for calibration. The X-ray lines measured were Ag Lα, Sb Lα, As Lα, Pb Lα, Zn Lα, Sn Lα, Fe Kα, Cu Kα, Se Kα, and S Kα. X-ray element mapping was performed using the energy-dispersive X-ray detector. The dwell time was set to 20 μs to provide the highest possible resolution.

Whole rock geochemistry

Eleven rock samples collected from drill cores and underground tunnels in the Shuangjianzishan ore district were analyzed for their whole rock compositions. The samples comprise fine-grained granite porphyry (4), coarse-grained granite porphyry (3), diorite to granodiorite dikes (2), granite (1) and dacite (1). Powders of the samples were prepared by crushing with corundum plates and grinding in an agate disk mill at the Hebei Geological Survey, China. Major element concentrations were analyzed by ICP-OES, and trace element concentrations by ICP-MS (Agilent-7500a) at CUGB. The precision for the major elements, as determined by the reproducibility of laboratory standards and duplicates, was better than 1%, with the exception of TiO_2 (~1.5%) and P_2O_5 (~2.0%), and for minor and trace elements was better than 10%. The results of the analyses are reported in Table 1. Most of the samples analyzed in this study are relatively fresh and have low loss on ignition (LOI; ≤ 1.5 wt.%), except for the two diorite-granodiorite dikes and the dacite, both of which were altered.

In situ S and Pb isotopes

Fifteen samples were collected for in situ sulfur and lead isotope analysis from several mining levels and drill cores, and are representative of the variety of mineralization in the Ag-Pb-Zn veins. Prior to

analysis, the thin sections were carefully observed with an optical microscope and FESEM, and analyzed with an electron microprobe (EPM) to establish the textural relationships and determine mineral compositions. Sulfur and lead isotopes were analyzed using a femtosecond laser ablation coupled multi-collector inductively coupled plasma mass spectrometer (fsLA-MC-ICP-MS) at the State Key Laboratory of Continental Dynamics, Northwest University, China. Details of the analytical methods for S and Pb isotopes have been reported by Chen, L., et al. (2017) and Yuan et al. (2015), respectively. These analyses were supplemented by analyses carried out using a 266 nm NWR UP Femto, femtosecond (fs) laser ablation system (ESI, U.S.A.) coupled to Nu Plasma 1700 (NP-1700) and Nu Plasma II (NP-II) MC-ICP-MS (Nu Instruments, Wrexham, U.K.), respectively. The surfaces of the polished thin sections were cleaned with milli-Q water (18.2 MΩ·cm). Argon flow rates and voltage were adjusted to give the best signal stability and intensity. Each sample acquisition consisted of background collection for 30 s, followed by ablation signal collection for 70 s, and a wash time of 50 s to reduce memory effects. The analyses employed a relatively low laser energy (the fluence ranged from 0.5 to 3.5 J cm^{-2}), a 10 Hz frequency and an ablation rate of 2 μm/s. The spot size for sulfur and lead were 20-37 and 9-40 μm, respectively. Instrument drift and mass bias were corrected using a sample-standard bracketing approach with repeated measurement of the standard before and after each sample. The international standard, NBS123 (sphalerite) and internal standards of PY-4 (pyrite), CBI-3 (galena), PSPT-3 (sphalerite), CPY-1 (chalcopyrite), and IAEA-S-1 (Ag_2S) were used for calibration in the sulfur isotope analyses. The analytical precision calculated from replicate analyses of unknown samples is better than 0.2‰ (1σ). The measured $\delta^{34}S_{VCDT}$ value of 17.8 ± 0.3‰ (n=156) for standard NBS123 is consistent with the reported value of 17.4 ± 0.2‰ (Craddock et al., 2008). The Tl NIST SRM 997 (20 ppb, $^{205}Tl/^{203}Tl$ = 2.38890) and NIST SRM 610 glass were used as internal and external Pb isotope standards, respectively. Repeated analyses of the NIST SRM 610 glass standard yielded highly reliable and reproducible results with mean $^{206}Pb/^{204}Pb$, $^{207}Pb/^{204}Pb$, and $^{208}Pb/^{204}Pb$ ratios of 17.050 ± 0.004, 15.510 ± 0.002, and 36.985 ± 0.006 (1σ, n = 63), respectively, which are very close to the reported reference ratios (Stern and Amelin, 2003).

Zircon U-Pb dating

Five rock samples were selected for zircon U-Pb dating. These comprise granite porphyry (fine- and coarse-grained) (Fig. 3A), granite intrusion (~2 km north of the vein system), diorite dike and dacite (Fig. 3B). Zircon crystals from the selected samples were separated by standard heavy-liquid and magnetic techniques, followed by hand-picking under a binocular microscope. Prior to LA-ICP-MS analysis, the

zircon crystals were imaged by cathodoluminescence (CL) with a FESEM at Peking University. The U-Pb age determinations were carried out using a LA-ICP-MS in the State Key Laboratory of Geological Processes and Mineral Resources at CUGB. The crystals were ablated using an excimer laser ablation system (UP193SS). An Agilent 7500a ICP-MS instrument was used to acquire ion-signal intensities. A laser spot size of 36 μm, laser energy density of 8.5 J/cm^2 and a repetition rate of 10 Hz were applied during analysis. Helium and argon were used as the carrier and make-up gases, and were mixed via a T-connector before entering the ICP-MS. Uranium, Th and Pb concentrations were calibrated by using ^{29}Si as an internal standard and NIST 610 glass as the reference standard. The ^{207}Pb/^{206}Pb, ^{206}Pb/^{238}U, ^{207}Pb/^{235}U and ^{208}Pb/^{232}Th ratios were calculated using the GLITTER 4.4.1 software and corrected for both instrumental mass bias and depth-dependent elemental and isotopic fractionation using Harvard zircon 91500 as the external standard (Wiedenbeck et al., 1995). The zircon standard, TEMORA, was used as a secondary standard to monitor the deviation of the age measurement/calculation (Black et al., 2003). The Harvard zircon 91500 and TEMORA zircon standards yielded weighted mean ages of 1062.5 ± 0.5 and 418.0 ± 6.9 Ma, respectively, which are very similar to the reported ages (i.e., 1065 and 417 Ma; Wiedenbeck et al., 1995; Black et al., 2003). Isoplot 3.0 was used to calculate the U-Pb ages and to make the Concordia plots (Ludwig, 2003).

Molybdenite and pyrite Re-Os dating

Three molybdenite-quartz veins/veinlets (0.5-2 cm) in the altered slate above the granite porphyry were analyzed for their molybdenite Re-Os isotope ratios (Fig. 3A). To date, no molybdenite has been found in the Ag-Pb-Zn mineralized veins. The grain size of the molybdenite typically ranges from 0.1 to 0.3 mm (Fig. 3A). The Re-Os ratios of four pyrite separates from the main Ag-Pb-Zn veins sampled at depths of 240 to 410 m were also analyzed (Fig. 3B). The pyrite grain-size ranges from 3 to 5 mm. The mineral separates of both the molybdenite and pyrite samples were obtained using conventional methods (i.e., crushing, washing, sieving, magnetic separation, and heavy liquid separation) followed by hand picking under a binocular microscope.

The rhenium-osmium analyses were carried out at the Laboratory for Sulfide and Source Rock Geochronology and Geochemistry at Durham University, United Kingdom. For molybdenite, a weighed aliquot (~21 to 61 mg) of the mineral separate plus a known amount of spike solution (^{185}Re + isotopically normal Os) were loaded into a Carius tube with 11N HCl (1 ml) and 15.5N HNO_3 (3 ml), sealed, and digested at 220°C for ~24 h. For pyrite, ~0.4 g of sample, together with a mixed spike of

^{185}Re + ^{190}Os, were loaded into a Carius tube with 11N HCl (3 ml) and 15.5N HNO_3 (6 ml), sealed, and digested at 220°C for ~24 h. For both sample types, Os was purified from the acid medium using solvent extraction ($CHCl_3$) at room temperature and microdistillation methods. The Re fraction was purified by NaOH-solvent extraction and anion chromatography. The Re and Os isotopic compositions were measured by negative thermal ionization mass spectrometry (N-TIMS) using a Thermo Scientific TRITON mass spectrometer; the Re and Os isotope compositions were measured using the static Faraday collection mode for molybdenite, and SEM in peak hopping mode for the pyrite Os fraction. All Re-Os uncertainties are reported at the 2σ absolute level, which followed the propagation of uncertainties related to Re and Os mass spectrometer measurements, blank determinations, spike and standard isotopic compositions, and calibration uncertainties of ^{185}Re and ^{187}Os. During the analyses, the Re and Os blanks were < 2.5 and 0.1 pg, respectively, and the ^{187}Os/^{188}Os ratio of the blank was 0.22 ± 0.02. Results of analyses of the Henderson molybdenite reference material (RM8599 - 27.695 ± 0.038 Ma) provided by Li et al. (2017) overlapped with those of this study. A ^{187}Re decay constant of 1.666×10^{-11} y^{-1} with an uncertainty of 0.31% was used in the calculation of the Re-Os dates (Smoliar et al., 1996; Selby et al., 2007).

Results

Ore mineralogy and paragenesis

Crosscutting relationships involving the different types of veins and textural relationships among the ore and gangue minerals show that the Ag-Pb-Zn mineralization at Shuangjianzishan occurred in three discrete stages (Fig. 4C, D): an early pyrite+quartz±K-feldspar stage (I), a sulfide+sulfosalt+quartz+calcite+sericite+chlorite±epidote stage (the main ore stage II) and a late quartz stage (III) (Fig. 5). The quartz-pyrite±K-feldspar assemblage occurs mainly in thin veins/veinlets (~2 to 10 mm in width) accompanied by potassic alteration halos (K-feldspar), and pyrite less commonly occurs as disseminations in the silicified slate. Pyrite in these veins/veinlets is relatively coarse-grained (~0.1 mm in diameter) and euhedral, occurring either as cubes or pyritohedra. The early veins/veinlets were crosscut, replaced or included as fragments in the main ore stage veins (Fig. 4C), in which sphalerite, galena, pyrite, quartz and calcite are the main minerals and are accompanied by subordinate proportions of Ag-bearing minerals and chalcopyrite. The main ore stage has been further subdivided into substages II-1 and II-2 (Fig. 5). Substage II-1 is represented by the ore mineral assemblage of galena+sphalerite+pyrite+chalcopyrite±canfieldite±freibergite and an alteration/gangue assemblage of

quartz+calcite+chlorite±epidote±sericite. This substage corresponded to a period of abundant sulfide deposition but minor Ag mineralization. The EPM results reveal that the base metal sulfides commonly do not contain any silver (Electronic Appendix Table A1), indicating that silver mineralization was very limited in the early Substage II-1.

The main Ag stage was Substage II-2, which is represented by Ag-bearing sulfosalts and argentite±galena±sphalerite±chalcopyrite and an alteration/gangue assemblage of quartz+sericite±calcite±chlorite (Fig. 5). Although we have subdivided the main ore stage into two substages, it is noteworthy that both substages can be observed in the same veins, suggesting that they belong to a single continuous stage (Fig. 5). Chemically, the paragenesis for the mineralization corresponds to an evolution from Fe-S through Pb-Zn-Fe-Cu-S to Ag-Cu-Sn-Sb-Se-S (Fig. 5).

The Ag-bearing minerals crystallized in Substage II-2. In order of relative abundance, they are canfieldite (Ag_8SnS_6), argentite (Ag_2S), freibergite [$(Ag, Cu)_{10}(Fe, Zn)_2Sb_4S_{13}$], polybasite ($Ag_9CuS_4Ag_4Cu_2Sb_{1.25}As_{0.75}S_7$), pyrargyrite ($Ag_3SbS_3$), and stephanite ($Ag_5SbS_4$). Minor native silver and electrum also have been observed (Wu et al., 2014). The other minor sulfides in this substage generally do not contain Ag, except for galena, which may contain up to 7 wt.% Ag but more typically contains <0.5 wt.% Ag.

Canfieldite, argentite and freibergite are the most abundant Ag-bearing ore minerals in the deposit, making up >80 vol.% of the Ag budget based on petrographic observations. Canfieldite is usually associated with argentite and freibergite, both of which commonly are associated with the earlier sulfides (e.g., sphalerite and galena) along their crystal boundaries (Fig. 6A-D), or occur interstitially to base metal sulfides (e.g., sphalerite and chalcopyrite; Fig. 6A, B), showing that these Ag-bearing minerals formed late relative to the base metal sulfides. Canfieldite has Ag, Sn, and S contents that range from 59.7 to 69.4, 9.5 to 19.3, and 10.6 to 21.3 wt.%, respectively (Electronic Appendix Table A1). The selenium content varies from below the detection limit (0.01 wt.%) to 11.6 wt.% (Zhai et al., 2019c), and is heterogeneously distributed within individual crystals (Fig. 7). Canfieldite is the only mineral that contains significant Se. There are also minor to trace amounts of Cu, Fe, and Te.

Argentite commonly replaced Stage II-1 sulfides, mainly sphalerite, galena (Fig. 6A), and chalcopyrite (Fig. 6B), and is intergrown with sericite and quartz; larger grains (>100 μm) commonly enclose the base metal sulfides (e.g., chalcopyrite and galena; Fig. 6E). Argentite also occurs in fine veinlets (20 to 50 μm wide) that crosscut argentian galena (Fig. 6F). The Ag content of the argentite ranges from 71.8 to 84.5

wt.%. There are also minor proportions of Sb and As, and in some cases Se. Freibergite, which as noted above, is commonly associated with canfieldite (Fig. 6C, D), is intergrown with or replaced base metal sulfides, particularly galena (Fig. 6F-H). It occurs both as large grains (e.g., >200 μm) and small cuspate-shaped irregular inclusions in galena (Fig. 6F, G); these galena-hosted inclusions also include pyrargyrite and minor pyrrhotite (Fig. 6G). The Ag, Cu and Sb contents of the freibergite vary from 19.4 to 42.1 wt.%, 11.9 to 25.1 wt.% and 19.3 to 25.8 wt.%, respectively, which span the compositional range from argentian tetrahedrite to freibergite. There are also significant concentrations of Fe (1.0 to 5.1 wt.%) and Zn (0.6 to 4.3 wt.%). The tennantite component is small (0.8 to 1.4 wt.% As). Among the remaining Ag minerals, pyrargyrite is the most important phase and commonly occurs as intergrowths with galena and in rare cases traces with pyrrhotite (Fig. 6G). Lesser proportions of stephanite and polybasite occur as intergrowths with freibergite and replaced galena and sphalerite (Fig. 6H, I).

Lithogeochemistry

Compositionally, the granite and granite porphyry are very similar and plot in the subalkaline granite field on a TAS discrimination diagram (Electronic Appendix Fig. A1). In chemical affinity, the porphyry varies from metaluminous to peraluminous (Electronic Appendix Fig. A2F), and belongs to the high-K calc-alkaline family (Electronic Appendix Fig. A2E). The fine-grained granite porphyry has the highest SiO_2 content among all the analyzed samples (mostly due to the silicic alteration), i.e., from 75.7 to 80.0 wt.%, whereas the SiO_2 content of the coarse-grained granite porphyry varies from 69.6 to 70.0 wt.%. Both the fine- and coarse-grained granite porphyry samples have similarly high K_2O contents, from 4.0 to 4.9 wt.%, whereas the Na_2O content of the coarse-grained porphyry is considerably higher (4.1 to 4.6 wt.%) than that of the fine-grained porphyry (2.2 to 3.7 wt.%). The K_2O content for both facies increases and the Al_2O_3, CaO, MgO, FeO^T, TiO_2 and P_2O_5 contents decrease with increasing SiO_2 content (Electronic Appendix Fig. A2A-E), as is the case for subalkaline granite suites globally (Whalen et al., 1987). The dacite sample has a relatively low silica content (65.0 wt.% SiO_2), and the two samples of diorite to granodiorite dikes also have low but variable silica contents (54.2 and 67.3 wt.% SiO_2), due possibly to the effects of hydrothermal alteration, as suggested by their relatively high LOI (2.6 to 4.1 wt.%; Table 1).

The granite porphyry samples (both fine-grained and coarse-grained) have relatively low Sr/Y (<10) and La/Yb (<20) values, low Sr (mostly <300 ppm), Rb (mostly <300 ppm) and Nb (mostly <20 ppm) contents, and high Y contents (mostly >30 ppm) (Table 1). They also have chondrite-normalized profiles

that display moderate enrichment of the light REE and negative Eu anomalies ($Eu_n/Eu^* < 0.7$) (Electronic Appendix Fig. A3A); the average $[La/Yb]_N$ is 7.0 ± 3.4 (n = 21). The fine-grained porphyry, however, has a more negative Eu anomaly ($Eu_n/Eu^* < 0.2$) than the coarse-grained facies ($Eu_n/Eu^* > 0.3$). Both porphyry facies are relatively depleted in Ba, Nb, Sr, P, Eu, and Ti, and enriched in U, La, and Nd relative to primitive mantle (Electronic Appendix Fig. A3B).

In situ S and Pb isotope compositions

The range of $\delta^{34}S$ values for all the sulfides and sulfosalts is relatively restricted, from -4.67 to +2.44‰ (Figs. 8, 9A) and largely independent of the depth in the deposit from which the samples were taken. Moreover, those for sphalerite (mean = -1.41‰), pyrite (mean = -1.27‰), chalcopyrite (mean = -1.58‰) and arsenopyrite (mean = -1.34‰) are comparable to the values for freibergite (mean = -1.17‰) and canfieldite (mean = -1.54‰) (Table 2). The $\delta^{34}S$ values for galena (mean = -3.58 ‰), however, are somewhat lower (Fig. 9A, B) and those for pyrargyrite are significantly higher (mean = +2.0‰). The $\delta^{34}S$ values decrease in the order of pyrite > sphalerite > chalcopyrite > galena based on the analyses of a given assemblage in the same ore stage, which is consistent with the experimentally determined equilibrium sulfur isotope fractionation factors for ^{32}S and ^{34}S between the fluid and sulfide minerals (Seal, 2006, and references therein) and likely indicates contemporaneous deposition of these sulfides from the ore fluid.

Interestingly, there is a small but significant variation in the sulfur isotopic composition within single crystals of most of the sulfides and sulfosalts. For example, the $\delta^{34}S$ value of the galena crystal shown in Figure 8A varies from -4.51 to -3.11‰ and for the crystal shown in Figure 8B varies from -3.79 to -3.22‰. The variation in the $\delta^{34}S$ values within the freibergite grains is somewhat smaller; for example, it is -1.72 to -1.35‰ for the grain shown in Figure 8C. In contrast, the variation is larger (+1.41 to +2.44‰) for pyrargyrite, as shown by the data for the grain in Figure 8D.

All the sulfides and sulfosalts analyzed have very similar lead isotope values (Fig. 10A, B; Table 3). The $^{206}Pb/^{204}Pb$, $^{207}Pb/^{204}Pb$ and $^{208}Pb/^{204}Pb$ ratios range from 18.243 to 18.310, 15.503 to 15.563, and 38.053 to 38.203, and the mean ratios are 18.279, 15.537 and 38.143, respectively (Table 3). These ratios do not vary significantly with the mineral or its depth in the deposit. The $^{206}Pb/^{204}Pb$ ratio varies linearly with the $^{207}Pb/^{204}Pb$ ratio (Fig. 10A) and with the $^{208}Pb/^{204}Pb$ ratio (Fig. 10B); the R^2 values are 0.877 and 0.786, respectively.

Zircon U-Pb ages

The zircon LA-ICP-MS U-Pb isotope determinations are reported in Electronic Appendix Table A2. The diorite dike that is crosscut by Ag-Pb-Zn veins (Fig. 3B) has a weighted mean zircon $^{206}Pb/^{238}U$ age of 250.2 ± 2.0 Ma (N = 19, MSWD = 0.3; Fig. 11A), showing that it was emplaced in the Early Triassic. This age is indistinguishable, within the uncertainty, from those reported previously for similar diorite dikes using the same methodology, i.e., 254 ± 3 to 249 ± 2 Ma (Cui, 2015; Liu, C., et al., 2016). The dacite, which was cut by several Ag-Pb-Zn mineralized quartz veins (Figs. 2A and 3B), yielded a mean zircon $^{206}Pb/^{238}U$ age of 133.9 ± 1.4 Ma (N = 22, MSWD = 0.43; Fig. 11B) and thus formed in the early Cretaceous instead of the Jurassic, as previously assumed (Wu et al., 2014). The granite in the northern part of the district (~2 km; Fig. 2A) yielded a mean zircon $^{206}Pb/^{238}U$ age of 135.2 ± 1.4 Ma (N = 20, MSWD = 0.06; Fig. 11C), which is indistinguishable within the uncertainty from that previously reported (133.7 ± 0.6 Ma; Wu, 2014). Identical zircon ages of 134.4 ± 1.0 (N = 21, MSWD = 0.1; Fig. 11D) and 134.4 ± 1.0 Ma (N = 21, MSWD = 0.2; Fig. 11E) were obtained for the coarse- and fine-grained granite porphyry, respectively. These zircon $^{206}Pb/^{238}U$ ages are very similar to those reported by Zhang (2018) of 134.4 ± 1.7 and 135.9 ± 1.1 Ma for samples from the drill hole (ZK12-37) considered in the current study, and are very similar to the zircon $^{206}Pb/^{238}U$ age of another concealed granite porphyry (133.4 ± 1.2 Ma; Gu et al., 2017) intersected in drill hole ZK12-50 ~3 km east of the vein system.

Molybdenite and pyrite Re-Os ages

The Re concentrations of the three molybdenite samples range from 0.12 to 2.61 ppm and the measured ^{187}Re and ^{187}Os values range from 0.07 to 1.66 ppm and 0.17 to 3.77 ppb, respectively (Table 4). The model ages for these samples are comparable, varying from 136.3 ± 0.9 to 133.7 ± 1.2 Ma; the weighted mean age is 134.9 ± 3.4 Ma (MSWD = 9; Table 4). These ages are, within the uncertainty, identical to the zircon $^{206}Pb/^{238}U$ ages of the porphyry and the other granitic intrusions in the district.

The Re and Os concentrations in the four pyrite samples range from 0.26 to 1.08 ppb and from 1.45 to 13.08 ppt (Table 5), and the $^{187}Re/^{188}Os$ and $^{187}Os/^{188}Os$ ratios from 496.9 to 34959.9 and 2.8 to 69, respectively (Table 5). Two of the samples yielded very high $^{187}Re/^{188}Os$ values (15SJ-16 = ~6300; 15SJ-114 = ~35000), indicating that the Os fraction is dominated by radiogenic ^{187}Os ($^{187}Os^{r}$) (Stein et al., 2000). Unfortunately, the Re-Os data did not return a meaningful isochron age for any of the pyrite samples. We interpret this to have been due to the highly variable initial $^{187}Os/^{188}Os$ ratio of the

samples, which may reflect multiple sources of Os (e.g., the porphyry and the host slates). Model Re-Os dates for three of the four pyrite separates, calculated using initial $^{187}Os/^{188}Os$ ratios varying from ~1.1 to 6.2, yielded a weighted mean age of 135.0 ± 0.6 Ma (MSWD = 9).

Discussion

Temperature of ore deposition

The temperature of ore deposition at Shuangjianzishan was estimated using a combination of ore mineral chemistry and stable isotope geothermometry. A temperature for the silver mineralization was estimated using the composition of freibergite and the fahlore geothermometer of Sack (2005), which was developed using an internally consistent thermodynamic database for the system Ag_2S-Cu_2S-ZnS-FeS-Sb_2S_3-As_2S_3. This geothermometer makes use of isotherms based on molar ratios of Ag/(Ag+Cu) and Zn/(Zn+Fe) in fahlore. Freibergite crystals, which show no evidence of having undergone post-mineralization solid-state reaction and exsolution (Zhai et al., 2019a), were selected for fahlore geothermometry. In addition, application of the fahlore geothermometer was restricted to freibergite crystals with Ag/(Ag+Cu) molar ratios < 0.55 because of the close spacing of the isotherms at higher ratios and the resulting high uncertainty of the corresponding temperature estimates. The temperatures estimated using this geothermometer ranged from ~200° to 280 °C and the mean temperature was ~240 °C (n = 9, Fig. 12).

The mineral pairs sphalerite-galena, pyrite-galena, pyrite-sphalerite, pyrite-chalcopyrite, chalcopyrite-galena and sphalerite-chalcopyrite were used to estimate temperature based on the fractionation of ^{32}S and ^{34}S between these sulfide minerals and the equations of Seal (2006). Only mineral pairs that were in apparent textural equilibrium were used. These mineral pairs (n = 19) yielded temperatures from 142° to >570°C. The highest temperatures were for pairs involving pyrite, a paragenetically early mineral. If these pairs are excluded, the range of temperature estimates using sulfur isotope geothermometry is from 210° and 320°C (Electronic Appendix Fig. A4) and the mean temperature is ~250°C.

In summary, the sulfur isotope and fahlore chemical geothermometers yielded temperatures ranging from 210° to 320°C (mean ~250°C) and 200° to 280 °C (mean ~240°C) for the base metal and silver mineralization, respectively, suggesting that base metal sulfides and Ag-bearing sulfosalts precipitated from an intermediate- to low-temperature hydrothermal fluid. These temperatures are similar to the homogenization temperatures of fluid inclusions hosted in quartz reported by Wang, X. (2017), which

are from 170° to 260°C for the base metal sulfide and silver mineralization.

Unusual features of the mineralogy

An unusual feature of the Shuangjianzishan deposit is that canfieldite (Ag_8SnS_6) is one of the main silver minerals (Fig. 6A-D). Significantly, the canfieldite has an unusually high Se content (up to 11.6 wt.%; Zhai et al., 2019c), which is zonally distributed such that the highest concentration is in the cores of crystals (Fig. 7D). Another unusual feature of the mineralogy is the occurrence of cassiterite (Fig. 7A, E; see also Jiang et al., 2018), which was replaced by canfieldite, argentite, galena and sphalerite (Fig. 7A). The element suite of the ore minerals of the Shuangjianzishan deposit therefore differs from that of the Ag-Pb-Zn veins associated with porphyry deposits in the North and South American Cordillera (e.g., Peru), which does not include significant Sn or Se (Bendezú and Fontboté, 2009).

We interpret the enrichment of Sn and Se in the Shuangjianzishan deposit to be of magmatic origin (as we do for the other ore elements; see below). In support of this interpretation, we note that Sn- and Se-bearing ore minerals also have been reported from several Ag-Au-Cu-Se-Te epithermal deposits that are spatially associated with porphyry deposits (e.g., the Prasolovskoye deposit, Kuril Islands, So et al., 1995; the Kawazu deposit, Japan, Shimizu et al., 2008; the Svetloye deposit, Russia, Alderton and Brameld, 2006; and the Mavrokoryfi prospect, Greece, Voudouris, 2011). It is also noteworthy that Se has been observed in the structure of molybdenite in intrusion-related deposits in Bohemia (Pasava et al., 2016), indicating a magmatic origin for the Se in these deposits. Finally, we note that a number of magmatic-hydrothermal ore deposits located relatively close to the Shuangjianzishan deposit, for example, the Bianjiadayuan Ag-Pb-Zn deposit, the Weilasituo Cu-Zn deposit, the Huangganglang Fe-(Sn) deposit, the Dajing Cu-Sn deposit, the Baiyinnuoer Pb-Zn deposit, the Haobugao Fe-Zn deposit, and the Anle Cu-Sn deposit (Fig. 1C), are spatially associated with Sn-rich granitic intrusions/porphyries and may be genetically related to them (Ouyang et al., 2015; Zhu et al., 2016; Zeng et al., 2016; Zhai et al., 2017).

Sulfur and metal sources

The sulfides and sulfosalts from the Ag-Pb-Zn mineralized veins at Shuangjianzishan have a narrow range of $\delta^{34}S$ values (i.e., -4.67 to +2.44‰) and an average value that is close to zero (Fig. 9A). Moreover, these values are independent of the mineral paragenesis (Fig. 9A) and the depth from which the samples were taken (Fig. 9B; Table 2). The corresponding range and mean $\delta^{34}S_{H2S}$ values are -3.32 to +0.77‰ and -1.65 ± 0.83‰, respectively, assuming a temperature of 250 °C. These observations suggest a magmatic source for the sulfur (Seal, 2006). The $\delta^{34}S$ values reported here are also very similar to

those of sulfides in nearby magmatic-hydrothermal ore deposits (e.g., the Bianjiadayuan Ag-Pb-Zn, Weilasituo Zn-Cu-Ag, Baiyinnuoer Pb-Zn, Hashitu Mo, Haobugao Fe-Zn, and Huanggangliang Fe-Sn deposits), which are generally in the range −4 to +4‰ (Yao et al., 2012; Ouyang et al., 2014; Zhai et al., 2014b, 2018b, 2019a, and references therein). This suggests strongly that most of the ore deposits in the southern GHR had a similar source of sulfur, namely a magma. Finally, we note that the relatively small range in the $\delta^{34}S$ values of the Shuangjianzishan ores, the even smaller range for individual minerals (Fig. 9) and the very small intra-crystal variation of these values indicate that pH and particularly fO_2 did not vary significantly during ore formation (see Ohmoto, 1972; Wood, 1998; King et al., 2014).

In order to evaluate the source of the metals, we compared the lead isotope compositions of the sulfides and Ag-bearing sulfosalts from Shuangjianzishan with corresponding data for Mesozoic granite, andesite and basalt, Paleozoic granite, and Permian slate, as well as Pb isotope data for sulfides from numerous nearby magmatic-hydrothermal ore deposits (Electronic Appendix Table A3; Zhang et al., 1995, 2008; Shen and Fu, 1999; Chu et al., 2001; Cai et al., 2004; Wang, 2009; Zeng et al., 2009; Guo et al., 2010; Jiang et al., 2010; Shao et al., 2010; Yao et al., 2012; Wu et al., 2012; Zhai et al., 2014b, 2018b, 2019a). The $^{206}Pb/^{204}Pb$, $^{207}Pb/^{204}Pb$, and $^{208}Pb/^{204}Pb$ ratios for the Shuangjianzishan ore minerals are very similar to those of magmatic-hydrothermal ore deposits in the region (Fig. 13A, B), suggesting strongly that the Shuangjianzishan ores and these deposits shared a common source for their metals. It should be noted, however, that the ranges for our ratios, which were obtained by in situ analysis, are significantly smaller than for the other deposits. We attribute this to the fact that the latter data were obtained from mineral separates. The ranges for our Pb isotope ratios are also narrower than those for the Shuangjianzishan deposit reported by Wang, F. (2017) from mineral separates; the latter ratios also indicate more radiogenic Pb isotope compositions (Electronic Appendix Fig. A5). We consider it likely that this difference is due to contamination of the separates by minerals with radiogenic Pb (e.g., sericite and K-feldspar).

The Pb isotopic ratios of the Shuangjianzishan ore minerals closely match those of the local Mesozoic (late Jurassic to early Cretaceous) granites (Fig. 13A, B). This suggests that the Pb and other metals (e.g., Ag and Zn) originated mainly from Mesozoic magmas (e.g., the Mo-mineralized porphyry). In contrast, the substantial differences between the Pb isotopic ratios of the Shuangjianzishan ore minerals and those of the other rock units in the district, for example, the Mesozoic basalt, andesite, the Paleozoic

granite and the Permian slate (Fig. 13A, B), demonstrate that these rock units did not contribute to the ore metal budget.

pH and fO_2 conditions

The pH-logfO_2 conditions of ore formation and alteration were evaluated from phase equilibria calculated using the HCh software package (Shvarov, 2011). Stability relationships among the minerals were determined assuming that the minerals are all ideal solid solutions. The total sulfur activity (ΣaS) was conservatively assumed to be 0.01 (e.g., Bonsall et al., 2011; Williams-Jones and Migdisov, 2014), the $\delta^{34}S_{\Sigma S}$ was assumed to be +0.5‰ (i.e., the isotopic composition of magmatic sulfur species), and the total dissolved CO_2 (ΣC) was assumed to be 1 m (e.g., Ohmoto, 1972). The temperatures evaluated were 250° and 200°C (see earlier discussion of the temperature of ore formation).

The pH of base metal sulfide and Ag-sulfosalt deposition at 250°C varied from 5.6 to 6.7 (pure water at this temperature has a pH value of 5.6) (Fig. 14A), based on the observation that this mineralization was associated with sericitization (Fig. 6A, I) and the occurrence of calcite as a gangue mineral (Fig. 4C). The presence of calcite also restricts logfO_2 to values above -43.1 and that of pyrite to values below -32.5 (Fig. 14A). The measured $\delta^{34}S$ values calculated to have been in equilibrium with the fluid for different sets of pH and logfO_2 conditions ($\delta^{34}S$ = −4.67 to +2.44‰; Fig. 9A) further restricts logfO_2 to values below -36.8 (Fig. 14A). These values correspond to ΔlogfO_2 (HM) values (hematite/magnetite buffer) of -8.7 to -2.4. At 200°C, the pH of base metal sulfide and Ag-sulfosalt deposition would have been 5.3 to 6.8 (the pH value of pure water at this temperature is 5.6) and the ΔlogfO_2 (HM) values would have been -8.5 to -2.2 (Fig. 14B). Thus, the fO_2 conditions of Ag-Pb-Zn ore deposition varied from moderately to strongly reducing; the pH was nearly neutral to weakly alkaline.

Timing of Ag-Pb-Zn mineralization

The age of vein-type Ag-Pb-Zn mineralization in the GHR is still poorly constrained, whereas that of spatially-associated porphyry Mo-Cu and skarn Fe-Sn deposits is well-known from numerous molybdenite Re-Os dates. Although there have been many determinations of the age of Ag-Pb-Zn mineralization in the Shuangjianzishan deposit, there is no agreement on this age. For example, Cui (2015) proposed an age of 249.1 ± 1.9 Ma for the deposit based on a zircon U-Pb age for one of the diorite dikes. As discussed earlier, however, these dikes predate the mineralization (Figs. 2A and 3B). Ouyang et al. (2016) proposed an age of 159.3 ± 2.3 Ma based on a zircon U-Pb date for a granite porphyry that they considered was related to the mineralization, whereas Gu et al. (2017), using the

same method applied to the porphyry, concluded that the mineralization developed at 133.4 ± 1.2 Ma. Wu et al. (2013) was the first to date the mineralization and obtained an age of 132.7 ± 3.9 Ma from a sphalerite Rb-Sr isochron. However, this Rb-Sr age was likely not the age of the sphalerite but rather the age of inclusions of a mineral such as muscovite that would have hosted the Rb and Sr. Wang et al. (2016) dated the mineralization indirectly by determining the age of sericite using the Ar-Ar method and obtained an age of 146.9 ± 1.9 Ma, but they did not establish the spatial and temporal relationships between the sericite and the mineralization. They also reported a Re-Os age of 162.6 ± 2.6 Ma for molybdenite from the nearby granite porphyry described earlier in this paper. More recently, Wang, F. (2017) obtained an age of 159 ± 6 Ma for the Ag-Pb-Zn mineralization using the Re-Os method applied to arsenopyrite and pyrite, and a U-Pb age of 148 ± 1 Ma for hydrothermal zircon.

As described earlier, we conducted a comprehensive geochronological program designed to reliably establish the age of the mineralization. The results of our determinations of the ages of the different lithological units in the Shuangjianzishan district are illustrated in Figure 15A. A diorite dike that is crosscut by the Ag-Pb-Zn veins and is pre-ore (Fig. 15B) yielded a zircon U-Pb age of 250.2 ± 2.0 Ma (Fig. 11A). Dacite located in the southwestern part of the district (Fig. 2A), which is cut by several Ag-Pb-Zn mineralized veins (Figs. 2A and 3B) and thus is also pre-ore, was dated at 133.9 ± 1.4 Ma (zircon U-Pb method, N = 22, MSWD = 0.43; Fig. 11B). Within the analytical uncertainty, the same age, 134.4 ± 1.0 Ma (Fig. 11D, E), was obtained for a Mo-mineralized granite porphyry located only 800 m from the deposit using the zircon U-Pb method, suggesting that the dacite and porphyry may have been derived from the same magma (Fig. 15C). Their similar trace element compositions also support this hypothesis (Electronic Appendix Fig. A3). Moreover, Re-Os dating of molybdenite related to the porphyry yielded a weighted mean age of 134.9 ± 3.4 Ma (MSWD = 9), which is indistinguishable within error from the age of the porphyry. Finally, a granite intrusion in the northern part of the mining district (~2 km from the deposit) yielded a mean $^{206}Pb/^{238}U$ age of 135.2 ± 1.4 Ma, which is indistinguishable within the uncertainty from the 133.7 ± 0.6 Ma age reported by Wu (2014) for the same intrusion.

We dated the Ag-Pb-Zn mineralization directly using the Re-Os model ages for the pyrite samples from the Ag-Pb-Zn mineralized veins (Fig. 3B). This yielded a weighted mean age of 135.0 ± 0.6 Ma that is in agreement with the sphalerite Rb-Sr isochron age of 132.7 ± 3.9 Ma reported by Wu et al. (2013). These ages, within the error, are the same as the ages reported for the granite porphyry and its

molybdenite mineralization (Fig. 15D). Based on these age determinations, we conclude that the Ag-Pb-Zn mineralization of the Shuangjianzishan deposit was the product of hydrothermal fluids released during an early Cretaceous felsic magmatic event at ~134 Ma (Fig. 15A). This event produced volcanic rocks (i.e., dacite) and granitic intrusions (Fig. 15C, D), including the nearby Mo-mineralized porphyry, which we speculate is genetically related to the Ag-Pb-Zn mineralization.

The age interpreted for the Shuangjianzishan deposit is similar to that for many other magmatic-hydrothermal ore deposits in the southern GHR (Fig. 1C). These include the Baiyinnuoer skarn Pb-Zn deposit (135 ± 1 Ma, molybdenite Re-Os; Ouyang et al., 2015), the Huangganglang skarn Fe-(Sn) deposit (135 ± 2 Ma, molybdenite Re-Os; Zhai et al., 2014b), the Weilasituo greisen Sn and Cu-Zn vein deposit (136 ± 1 Ma, zircon U-Pb; Zhai et al., 2016), the Bairendaba Ag-Pb-Zn vein deposit (135 ± 3 Ma, sericite Ar-Ar; Chang and Lai, 2010), the Anle Sn-(Cu) vein deposit (133 ± 3 Ma, sericite Ar-Ar; Wang et al., 2001), and the Dajing Cu-(Sn) vein deposit (133 ± 1 Ma, zircon U-Pb/sericite Ar-Ar; Ishiyama et al., 2008; Jiang et al., 2012). Shuangjianzishan is thus a representative of an important late Mesozoic (early Cretaceous) metallogenetic event in the southern GHR that involved felsic magmatism (Mao et al., 2005, 2014; Wu et al., 2011; Ouyang et al., 2015; Zhai et al., 2015; Shu et al., 2016; Chen, Y., et al., 2017).

Tectonic controls on Ag-Pb-Zn mineralization

The regional magmatism in the early Cretaceous is represented by both I-type (granodiorite, monzogranite and syenite) and A-type granitoids (Wu et al., 2002); the latter are interpreted to have formed from magmas derived from the lower crust (Wei et al., 2008). These granitoids display an eastward-younging trend, which indicates their emplacement in an extensional setting (Zhang et al., 2010; Wu et al., 2011). The granite porphyry in the Shuangjianzishan district has a geochemical signature characteristic of an arc-related magma (i.e., Y >30 ppm and Sr/Y ratios <10; Electronic Appendix Fig. A6A), but nonetheless one that is distinguishable from the adakites, which are commonly associated with porphyry Cu±Mo±Au deposits (Sun et al., 2011; Richards, 2011; Chiaradia et al., 2012). However, it also has characteristics typical of A-type granites forming in extensional tectonic settings (Electronic Appendix Fig. A6B). This setting for the GHR in the early Cretaceous is manifested by the development of extensional basins (e.g., the Songliao, Erlian, and Hailaer basins; Meng, 2003), formation of metamorphic core complexes (Wang et al., 2012), widespread alkali plutonism and volcanism (A-type granites and bimodal volcanic rocks; Wu et al., 2002; Wang et al., 2006; Zhang et al.,

2010), and formation of Climax-type porphyry molybdenum deposits (e.g., the Hashitu, Haisugou, Banlashan, and Aolunhua deposits; Zhai et al., 2018b) and alkaline intrusion-related rare metal deposits (e.g., the Baerzhe Zr, REE and Nb deposit; Ouyang et al., 2015). It has been proposed that Paleo-Pacific subduction in the early Cretaceous caused lithospheric delamination, slab rollback and crustal extension of the back-arc domain (Zhang et al., 2010; Wu et al., 2011, and references therein). The slab rollback could have triggered large scale upwelling of the asthenosphere and back-arc spreading along the entire margin of NE China, softening the lithosphere, thereby facilitating the lithospheric thinning and extension observed across the East Asian continental margin for the early Cretaceous (~140-110 Ma; Zhang et al., 2011). This, in turn, could have led to the emplacement of the large numbers of Cretaceous granitoids in NE China (Zhang et al., 2008; Wu et al., 2011; Wilde, 2015). In summary, we propose that the widespread synchronous Ag-Pb-Zn mineralization observed in the GHR, including the Shuangjianzishan deposit, was a direct consequence of Paleo-Pacific subduction and subsequent slab rollback, lithospheric delamination, thinning and extension that triggered the emplacement of large volumes of granitic magma during the early Cretaceous.

A Proposed Genetic Model

The data presented in this paper provide strong evidence that the Ag-Pb-Zn veins of the Shuangjianzishan deposit were the product of a magmatic-hydrothermal system related to a nearby early Cretaceous Mo-mineralized granite porphyry. These data show, moreover, that the mineralization was coeval with the intrusion of this porphyry. In Figure 15, we present a model that explains the genesis of the Shuangjianzishan Ag-Pb-Zn deposit using the geological observations and geochemical data presented earlier. In this model, both the ore-forming fluid and metals (i.e., Ag, Pb, and Zn) were sourced from the adjacent porphyry intrusion, which has an arc affinity (Electronic Appendix Fig. A6) and was emplaced in the early Cretaceous (Fig. 15A) in response to regional slab rollback and lithospheric delamination and thinning. The porphyry was intruded in two phases (early coarse-grained and late fine-grained phases), the second of which exsolved a magmatic-hydrothermal fluid. The metals and sulfur were transported to well beyond the confines of the intrusion (~ 800 m away) by this fluid, where they were deposited in pre-existing faults or fractures created by the withdrawal of magma during the waning stages of the magmatic-hydrothermal system (Fig. 15D).

The Shuangjianzishan ore district is similar in many aspects to Cordilleran ore districts, in which porphyry deposits are associated with distal Ag-Pb-Zn deposits (Fontboté and Bendezú, 2009;

Baumgartner et al., 2009), but there are also significant differences. The similarities include: ore (sulfide and a variety of Ag-bearing sulfosalts) and gangue (quartz and calcite) mineral assemblages; the ore paragenesis (base metal sulfides prior to Ag-bearing sulfosalts/sulfides); alteration zonation; high Ag/Au ratios; open space filling and epigenetic veins structurally controlled by faults; formation under epithermal conditions at shallow levels (<1 km) from low temperature (~200° to 250°C) and salinity (~1 to 10 wt.% NaCl equivalent) fluids; a magmatic source for the fluids and metal; and a close genetic association with porphyry systems (Baumgartner et al., 2009; Fontboté and Bendezú, 2009; Catchpole et al., 2015; Rottier et al., 2016, 2018a). An important difference is that the Cordilleran veins are commonly characterized by a Cu-Zn-Pb-(Ag-Au-Bi) metal suite (Fontboté and Bendezú, 2009), whereas the Shuangjianzishan deposit, as well as other Ag-Pb-Zn veins in the GHR, have a Ag-Pb-Zn-(Sn-Se-Sb) metal suite (Fig. 5); the Shuangjianzishan deposit is distinguished by rare Ag-bearing sulfosalts (i.e., canfieldite, Figs. 6A-D, 7), whereas the sulfosalts in the Cordilleran veins are dominantly Bi-bearing (e.g., cuprobismutite; Baumgartner et al., 2008). Moreover, a well-developed spatial zonation of ore and alteration minerals has been identified in many of the Cordilleran veins (Catchpole et al., 2015), whereas this is not observed in the Shuangjianzishan deposit and other Ag-Pb-Zn deposits in the GHR (Zhai et al., 2019a). Another significant difference is that the distal Ag-rich Peruvian deposits are hosted by carbonates (Fontboté and Bendezú, 2009), whereas the Shuangjianzishan deposit is hosted by slates (Fig. 2). The Cordilleran veins commonly formed in the shallow parts of porphyry Cu systems, in which both epithermal and porphyry-type mineralization are important (Baumgartner et al., 2008; Bendezú and Fontboté, 2009), whereas, although a close genetic relationship between the Shuangjianzishan Ag-Pb-Zn veins and a porphyry system has been established, the porphyry-type mineralization is very limited and other similar vein-type Ag-Pb-Zn deposits in the GHR are not associated with known porphyry-type mineralization. Finally, the GHR polymetallic vein deposits are related to post-subduction back-arc porphyry Mo systems, whereas the Cordilleran veins are commonly associated with subduction-related porphyry Cu systems (Fontboté and Bendezú, 2009; Catchpole et al., 2015). In conclusion, the model proposed for the giant Shuangjianzishan deposit emphasizes a genetic relationship between minor proximal Mo mineralization and considerable distal epithermal Ag-Pb-Zn mineralization. We expect that recognition of this relationship will provide an important guide for regional Ag-Pb-Zn exploration in NE China and elsewhere.

Acknowledgements

This research was supported financially by the National Natural Science Foundation of China (Grant 41672068), the Fundamental Research Funds for the Central Universities (Grants 2652015045, 2652018129 and QZ05201904), the MOST Special Fund from the State Key Laboratory of Geological Processes and Mineral Resources, China University of Geosciences (Grant MSFGPMR201804) and the Chinese "111" project (Grant B07011). We thank Li Su, Hongyu Zhang and Peng Xiang (CUGB) for performing the U-Pb analyses, Dongjie Tang (CUGB) for assistance with the SEM, and Zhenyu Chen and Xiaodan Chen (CAGS) for help with the microprobe analyses. Hegen Ouyang provided valuable insights into the ore deposit geology, and Xiaowen Huang helped with the interpretation of the Re-Os data. Meng Dai and Wenbin Jia assisted with the field work and sample collection. Preparation and writing of this manuscript was completed during DZ's visit to McGill University. Travel to and living expenses in Canada were supported financially by an international visiting program grant from the Fundamental Research Funds for the Central Universities, China. DS acknowledges the Total Endowment Fund and the CUG (Wuhan) scholarship. We thank Economic Geology reviewers Bertrand Rottier and Ryan Taylor, Associate Editor David John and Editor-in-Chief Larry Meinert for their insightful reviews, which helped improve this paper.

References

Alderton, D.H.M., and Brameld, F.C., 2006, Telluride mineralization at the Svetloye gold prospect, Khabarovsk Krai, eastern Russia. In: Cook NG, Özgenc I, Oyman T (eds) Au-Ag-Te-Se deposits, IGCP 486 field workshop, Izmir 24-29 September 2006, Proceedings, p. 1-5.

Balabin, A.I., and Sack, R.O., 2000, Thermodynamics of (Zn, Fe)S sphalerite: a CVM approach with large basis clusters: Mineralogical Magazine, v. 64, p. 923-943.

Baumgartner, R., Fontboté, L., and Vennemann, T., 2008, Mineral zoning and geochemistry of epithermal polymetallic Zn-Pb-Ag-Cu-Bi mineralization at Cerro de Pasco, Peru: Economic Geology, v. 103, p. 493-537.

Baumgartner, R., Fontboté, L., Spikings, R., Ovtcharova, M., Schaltegger, U., Schneider, J., Page, L., and Gutjahr, M., 2009, Bracketing the age of magmatic-hydrothermal activity at the Cerro de Pasco epithermal polymetallic deposit, central Peru: A U-Pb and $^{40}Ar/^{39}Ar$ study: Economic Geology, v. 104, p. 479-504.

Beaudoin, G., and Sangster, D.F., 1992, A descriptive model for silver-lead-zinc veins in clastic metasedimentary terranes: Economic Geology, v. 87, p. 1005-1021.

Bendezú, R., and Fontboté, L., 2002, Late timing for high sulfidation Cordilleran base metal lode and replacement deposits in porphyry-related districts: the case of Colquijirca, central Peru: SGA News, v. 13, p. 1-9.

Bendezú, R., and Fontboté, L., 2009, Cordilleran epithermal Cu-Zn-Pb-(Au-Ag) mineralization in the Colquijirca district, central Peru: Deposit-scale mineralogical patterns: Economic Geology, v. 104, p. 905-944.

Black, L.P., Kamo, S.L., Allen, C.M., Aleinikoff, J.N., Davis, D.W., Korsch, R.J., and Foudoulis, C., 2003, TEMORA 1: a new zircon standard for Phanerozoic U-Pb geochronology: Chemical Geology, v. 200, p. 155-170.

Bonsall, T.A., Spry, P.G., Voudouris, P.C., Tombros, S., Seymour, K.S., and Melfos, V., 2011, The geochemistry of carbonate-replacement Pb-Zn-Ag mineralization in the Lavrion district, Attica, Greece: Fluid inclusion, stable isotope, and rare earth element studies: Economic Geology, v. 106, p. 619-651.

Cai, J.H., Yan, G.H., Xiao, C.D., Wang, G.Y., Mu, B.L., and Zhang, R.H., 2004, Nd, Sr, Pb isotopic characteristics of the Mesozoic intrusive rocks in the Taihang Da Hinggan Mountains Tectonomagmatic Belt and their source region: Acta Petrologica Sinica, v. 20, p. 1225-1242 (in Chinese with English abstract).

Catchpole, H., Kouzmanov, K., Putlitz, B., Seo, J.H., and Fontboté, L., 2015, Zoned base metal mineralization in a porphyry system: Origin and evolution of mineralizing fluids in the Morococha district, Peru: Economic Geology, v. 110, p. 39-71.

Chang, Y., and Lai, Y., 2010, Study of characteristics of ore-forming fluid and chronology in the Yindu Ag–Pb–Zn polymetallic ore deposit, Inner Mongolia: Acta Scientiarum Naturalium Universitatis Pekinensis, v. 46, p. 581-593 (in Chinese with English abstract).

Chen, L., Chen, K., Bao, Z., Liang, P., Sun, T., and Yuan, H., 2017, Preparation of standards for in situ sulfur isotope measurement in sulfides using femtosecond laser ablation MC-ICP-MS: Journal of Analytical Atomic Spectrometry, v. 32, p. 107-116.

Chen, Y.J., Zhang, C., Wang, P., Pirajno, F., and Li, N., 2017, The Mo deposits of Northeast China: a powerful indicator of tectonic settings and associated evolutionary trends: Ore Geology Reviews, v. 81, p. 602-640.

Chiaradia, M., 2014, Copper enrichment in arc magmas controlled by overriding plate thickness: Nature Geoscience, v. 7, p. 43.

Chiaradia, M., Ulianov, A., Kouzmanov, K., and Beate, B., 2012, Why large porphyry Cu deposits like high Sr/Y magmas?: Scientific reports, v. 2, p. 685.

Chu, X.L., Huo, W.G., and Zhang, X., 2001, Sulfur, carbon and lead isotope studies of the Dajing polymetallic deposit in Linxi county, Inner Mongolia, China – Implication for metallogenic elements from hypomagmatic source: Resource Geology, v. 51, p. 333-344.

Craddock, P.R., Rouxel, O.J., Ball, L.A., and Bach, W., 2008, Sulfur isotope measurement of sulfate and sulfide by high-resolution MC-ICP-MS: Chemical Geology, v. 253, p. 102-113.

Cui, M., 2015, The geochemical characteristics and diagenesis of ore-forming diorite-porphyrite from Shuangjianzishan Ag polymetallic deposit in Inner Mongolia: Master thesis, China University of Geosciences Beijing, Beijing, China, 55 p. (in Chinese with English abstract).

Defant, M.J., and Drummond, M.S., 1993, Mount St. Helens: potential example of the partial melting of the subducted lithosphere in a volcanic arc: Geology, v. 21, p. 547-550.

Duan, X.X., Zeng, Q.D., Yang, Y.H., Liu, J.M., Chu, S.X., Sun, Y., and Zhang, Z.L., 2015, Triassic magmatism and Mo mineralization in Northeast China: geochronological and isotopic constraints from the Laojiagou porphyry Mo deposit: International Geology Review, v. 57, p. 55-75.

Einaudi, M.T., 1981, Skarns associated with porphyry plutons: Description of deposits, southwestern North America. II. General features and origin. Advances in Geology of the Porphyry Copper Deposits of Southwestern North America. University of Arizona Press, Tucson, p. 139-183.

Einaudi, M.T., Hedenquist, J.W., and Inan, E.E., 2003, Sulfidation state of fluids in active and extinct hydrothermal systems: transitions from porphyry to epithermal environments: Special Publication-Society of Economic Geologists, v. 10, p. 285-314

Fontboté, L., and Bendezú, R., 2009, Cordilleran or Butte-type veins and replacement bodies as a deposit class in porphyry systems. In: Williams et al., P.J. (ed) Proceedings of the 10th Biennial Society of Geology Applied to Ore Deposits Meeting, Townsville, Australia, p. 521-523.

Gao, J., Klemd, R., Zhu, M., Wang, X., Li, J., Wan, B., Xiao, W., Zeng, Q., Shen, P., Sun, J., and Qin, K., 2018, Large-scale porphyry-type mineralization in the Central Asian metallogenic domain: A review: Journal of Asian Earth Sciences, v. 165, p. 7-36.

Gu, Y.C., Chen, R.Y., Jia, B., and Ju, N., 2017, Zircon U-Pb dating and geochemistry of the granite porphyry

from the Shuangjianzishan silver polymetallic deposit in Inner Mongolia and tectonic implications: Geology and Exploration, v. 53, p. 495-507 (in Chinese with English abstract).

Guilbert, J.M., and Park, C.F., 1986, The geology of ore deposits, 4th ed.: New York, WH Freeman, 985 p.

Guo, F., Fan, W., Gao, X., Li, C., Miao, L., Zhao, L., and Li, H., 2010, Sr–Nd–Pb isotope mapping of Mesozoic igneous rocks in NE China: constraints on tectonic framework and Phanerozoic crustal growth: Lithos, v. 120, p. 563-578.

HBGMR (Heilongjiang Bureau of Geology and Mineral Resources), 1993, Regional Geology of Heilongjiang Province. Geological Publishing House, Beijing, pp. 347–418 (in Chinese with English abstract).

Heinrich, C.A., 2005, The physical and chemical evolution of low-salinity magmatic fluids at the porphyry to epithermal transition: a thermodynamic study: Mineralium Deposita, v. 39, p. 864-889.

Irvine, T.N.J., and Baragar, W.R.A.F., 1971, A guide to the chemical classification of the common volcanic rocks: Canadian Journal of Earth Sciences, v. 8, p. 523-548.

Ishiyama, D., Sato, R., Toshio, M., Yohei, I., and Wang, J.B., 2008, Characteristic features of tin-iron-copper mineralization in the Anle-Huanggangliangmining area, InnerMongolia, China: Resource Geology, v. 51, p. 377-392.

Jahn, B.M., 2004, The Central Asian Orogenic Belt and growth of the continental crust in the Phanerozoic. In: Malpas, J., Fletcher, C.J.N., Ali, J.R., Aitchison, J.C. (Eds.), Aspects of the tectonic evolution of China: Geological Society, London, Special Publications, v. 226, p. 73-100.

Jahn, B.M., Wu, F., and Chen, B., 2000, Granitoids of the Central Asian Orogenic Belt and continental growth in the Phanerozoic: Geological Society of America Special Papers, v. 350, p. 181-193.

Jensen, E.P., and Barton, M.D., 2000, Gold deposits related to alkaline magmatism: Reviews in Economic Geology, v. 13, p. 279-314.

Jiang, B., Wu, G., Chen, Y., Zhang, T., Liu, W., Zhang, T., and Li, X., 2018, Constraints on the genesis of the Shuangjianzishan silver-polymetallic deposit, Balinzuo Qi, Inner Mongolia: evidence from trace and rare earth elements: Acta Geologica Sinica, v. 92, p. 769-786 (in Chinese with English abstract).

Jiang, B.B., Zhu, X.Y., Huang, X.K., Xu, Q., and Zhang, Z.Q., 2017, Isotopic characteristics of sulfur and lead metallogenic mechanism of Shuangjianzishan silver polymetallic deposit in Inner Mongolia: Mineral Exploration, v. 8, p. 1010-1019 (in Chinese with English abstract).

Jiang, S.H., Chen, C.L., Bagas, L., Liu, Y., Han, N., Kang, H., and Wang, Z.H., 2017, Two mineralization events in the Baiyinnuoer Zn-Pb deposit in Inner Mongolia, China: Evidence from field observations, S-Pb isotopic compositions and U-Pb zircon ages: Journal of Asian Earth Sciences, v. 144, p. 339-367.

Jiang, S.H., Liang, Q.L., Liu, Y.F., and Liu, Y., 2012, Zircon U–Pb ages of the magmatic rocks occurring in and around the Dajing Cu–Ag–Sn polymetallic deposit of Inner Mongolia and constrains to the ore-forming age: Acta Petrologica Sinica, v. 28, p. 495–513 (in Chinese with English abstract).

Jiang, S.H., Nie, F.J., Liu, Y.F., and Yun, F., 2010, Sulfur and lead isotopic compositions of Bairendaba and Weilasituo silver-polymetallic deposits, Inner Mongolia: Mineral Deposits, v. 28, p. 101-112 (in Chinese with English abstract).

Whalen, J.B., Currie, K.L., and Chappell, B.W., 1987, A-type granites: geochemical characteristics, discrimination and petrogenesis: Contributions to Mineralogy and Petrology, v. 95, p. 407-419.

King, J., Williams-Jones, A.E., van Hinsberg, V., and Williams-Jones, G., 2014, High-sulfidation epithermal pyrite-hosted Au (Ag-Cu) ore formation by condensed magmatic vapors on Sangihe Island, Indonesia: Economic Geology, v. 109, p. 1705-1733.

Kissin, S.A., and Mango, H., 2014, Silver Vein Deposits. Treatise on Geochemistry, Second Edition. Elsevier, Oxford, p. 425-432.

Kuang, Y.S., Zheng, G.R., Lu, M.J., Liu, Y.L., Zhang, S.J., Li, R.Y., and Cheng, W.J., 2014, Basic characteristics of Shuangjianzishan silver polymetallic dposit in Chifeng City, Inner Mongolia: Mineral Deposits, v. 33, p. 847-856 (in Chinese with English abstract).

Li, J.Y., 2006, Permian geodynamic setting of Northeast China and adjacent regions: closure of the Paleo-Asian Ocean and subduction of the Paleo-Pacific Plate: Journal of Asian Earth Sciences, v. 26, p. 207-224.

Li, Y., Selby, D., Condon, D., and Tapster, S., 2017, Cyclic magmatic-hydrothermal evolution in porphyry systems: high-precision U-Pb and Re-Os geochronology constraints on the Tibetan Qulong porphyry Cu-Mo deposit: Economic Geology, v. 112, p. 1419-1440.

Liu, C., Bagas, L., and Wang, F., 2016, Isotopic analysis of the super-large Shuangjianzishan Pb–Zn–Ag deposit in Inner Mongolia, China: Constraints on magmatism, metallogenesis, and tectonic setting: Ore Geology Reviews, v. 75, p. 252-267.

Liu, K., Zhang, J., Wilde, S. A., Zhou, J., Wang, M., Ge, M., Wang, J., and Ling, Y., 2017, Initial subduction of the Paleo-Pacific Oceanic plate in NE China: Constraints from whole-rock geochemistry and zircon U-

Pb and Lu-Hf isotopes of the Khanka Lake granitoids: Lithos, v. 274-275, p. 254-270.

Liu, Y., Jiang, S., and Bagas, L., 2016, The genesis of metal zonation in the Weilasituo and Bairendaba Ag–Zn–Pb–Cu–(Sn–W) deposits in the shallow part of a porphyry Sn–W–Rb system, Inner Mongolia, China: Ore Geology Reviews, v. 75, p. 150-173.

Ludwig, K.R., 2003, User's Manual for Isoplot 3.0: a Geochronological Toolkit for Microsoft Excel: Berkeley Geochronology Centre, Special Publication.

Maniar, P.D., and Piccoli, P.M., 1989, Tectonic discrimination of granitoids: Geological Society of America Bulletin, v. 101, p. 635–643.

Mao, J., Pirajno, F., Lehmann, B., Luo, M., and Berzina, A., 2014, Distribution of porphyry deposits in the Eurasian continent and their corresponding tectonic settings: Journal of Asian Earth Sciences, v. 79, p. 576-584.

Mao, J.W., Xie, G.Q., Zhang, Z.H., Li, X.F., Wang, Y.T., Zhang, C.Q., and Li, Y.F., 2005, Mesozoic large-scale metallogenic pluses in North China and corresponding geodynamic settings: Acta Petrologica Sinica, v. 21, p. 169–188 (in Chinese with English abstract).

McDonough, W.F., and Sun, S.S., 1995, The composition of the Earth: Chemical Geology, v. 120, p. 223-253.

Meng, Q.R., 2003, What drove late Mesozoic extension of the northern China–Mongolia tract?: Tectonophysics, v. 369, p. 155-174.

Middlemost, E.A., 1994, Naming materials in the magma/igneous rock system: Earth-Science Reviews, v. 37, p. 215-224.

Ohmoto H., 1972, Systematics of sulfur and carbon isotopes in hydrothermal ore deposits: Economic Geology, v. 67, p. 551-578.

Ouyang, H., Li, R., and Zhou, Z., 2016, The Jurassic mineralization of the Shuangjianzishan Ag-polymetallic deposit and its significance in prospecting: evidence from geochronology: Acta Geologica Sinica, v. 90, p. 1835-1845 (in Chinese with English abstract).

Ouyang, H., Mao, J., Santosh, M., Wu, Y., Hou, L., and Wang, X., 2014, The Early Cretaceous Weilasituo Zn–Cu–Ag vein deposit in the southern Great Xing'an Range, northeast China: Fluid inclusions, H, O, S, Pb isotope geochemistry and genetic implications: Ore Geology Reviews, v. 56, p. 503-515.

Ouyang, H., Mao, J., Zhou, Z., and Su, H., 2015, Late Mesozoic metallogeny and intracontinental magmatism, southern Great Xing'an Range, northeastern China: Gondwana Research, v. 27, p. 1153-1172.

Pašava, J., Svojtka, M., Veselovský, F., Ďurišová, J., Ackerman, L., Pour, O., Drábek, M., Halodová, P., and Haluzová, E., 2016, Laser ablation ICPMS study of trace element chemistry in molybdenite coupled with scanning electron microscopy (SEM)—an important tool for identification of different types of mineralization: Ore Geology Reviews, v. 72, p. 874-895.

Pearce, J.A., Harris, N.B., and Tindle, A.G., 1984, Trace element discrimination diagrams for the tectonic interpretation of granitic rocks: Journal of Petrology, v. 25, p. 956-983.

Qi, J.P., Chen, Y.J., and Pirajno, F., 2005, Geological characteristics and tectonic setting of the epithermal deposits in the northeast China: Journal of Mineralogy and Petrology, v. 25, p. 47-59 (in Chinese with English abstract).

Richards, J.P., 2011, High Sr/Y arc magmas and porphyry Cu±Mo±Au deposits: just add water: Economic Geology, v. 106, p. 1075-1081.

Rickwood, P.C., 1989, Boundary lines within petrologic diagrams which use oxides of major and minor elements: Lithos, v. 22, p. 247-263.

Rottier, B., Kouzmanov, K., Casanova, V., Bouvier, A.S., Baumgartner, L.P., Wälle, M., and Fontboté, L., 2018a, Mineralized breccia clasts: a window into hidden porphyry-type mineralization underlying the epithermal polymetallic deposit of Cerro de Pasco (Peru): Mineralium Deposita, v. 53, p. 919-946.

Rottier, B., Kouzmanov, K., Casanova, V., Wälle, M., and Fontboté, L., 2018b, Cyclic dilution of magmatic metal-rich hypersaline fluids by magmatic low-salinity fluid: a major process generating the giant epithermal polymetallic deposit of Cerro de Pasco, Peru: Economic Geology, v. 113, p. 825-856.

Rottier, B., Kouzmanov, K., Wälle, M., Bendezú, R., and Fontboté, L., 2016, Sulfide replacement processes revealed by textural and LA-ICP-MS trace element analyses: example from the early mineralization stages at Cerro de Pasco, Peru: Economic Geology, v. 111, p. 1347-1367.

Rusk, B.G., Reed, M.H., and Dilles, J.H., 2008, Fluid inclusion evidence for magmatic-hydrothermal fluid evolution in the porphyry copper-molybdenum deposit at Butte, Montana: Economic Geology, v. 103, p. 307-334.

Sack, R.O., 2005, Internally consistent database for sulfides and sulfosalts in the system Ag_2S-Cu_2S-ZnS-FeS-Sb_2S_3-As_2S_3: Update: Geochim Cosmochim Acta, v. 69, p. 1157-1164.

Seal, R.R., 2006, Sulfur isotope geochemistry of sulfide minerals: Reviews in Mineralogy and Geochemistry, v. 61, p. 633-677.

Seedorff, E., Dilles, J.H., Proffett, J.M., Einaudi, M.T., Zurcher, L., Stavast, W.J.A., Johnson, D.A., and

Barton, M.D., 2005, Porphyry deposits: Characteristics and origin of hypogene features: Economic Geology 100th Anniversary Volume, p. 251-298.

Selby, D., Creaser, R.A., Stein, H.J., Markey, R.J., and Hannah, J.L., 2007, Assessment of the ^{187}Re decay constant by cross calibration of Re–Os molybdenite and U–Pb zircon chronometers in magmatic ore systems: Geochimica et Cosmochimica Acta, v. 71, p. 1999-2013.

Shao, J.A., Mu, B.L., Zhu, H.Z., and Zhang, L.Q., 2010, Material source and tectonic settings of the Mesozoic mineralization or the Da Hinggan Mts: Acta Petrologica Sinica, v. 26, p. 649-656 (in Chinese with English abstract).

Shen, J.F., and Fu, X.Z., 1999, The metallogenic environment and geology of copper polymetallic deposits in the Middle segment of Great Xing'an Range: Geological Publishing House, Beijing (in Chinese).

Shimizu, M., Shimizu, M., Furuhashi, T., Harada, A., and Cook, N., 2008, Indium mineralization in epithermal Au-Ag-Cu-Mn-Te-(Se-Bi-Sn-Mo-In) vein-type deposits of the Kawazu (Rendaiji) mine, Shizuoka Prefecture, Japan: Intern Geol Congr Olso, MRD-09 Au-Ag-telluride-selenide deposits, Abstract.

Shu, Q., Chang, Z., Lai, Y., Zhou, Y., Sun, Y., and Yan, C., 2016, Regional metallogeny of Mo-bearing deposits in northeastern China, with new Re-Os dates of porphyry Mo deposits in the northern Xilamulun district: Economic Geology, v. 111, p. 1783-1798.

Shvarov, Y., 2011, Unitherm Software, version 4.4.

Sillitoe, R.H, 2010, Porphyry copper systems: Economic geology, v. 105, p. 3-41.

Smoliar, M.I., Walker, R.J., and Morgan, J.W., 1996, Re-Os ages of group IIA, IIIA, IVA, and IVB iron meteorites: Science, v. 271, p. 1099-1102.

So, C.S., Dunchenko, V.Y., Yun, S.T., Park, M.E., Choi, S.G., and Shelton, K.L., 1995, Te- and Se-bearing epithermal Au-Ag mineralization, Prasolovskoye, Kunashir Island, Kuril Island arc: Economic Geology, v. 90, p. 105-117.

Stein, H.J., Morgan, J.W., and Scherstén, A., 2000, Re-Os dating of low-level highly radiogenic (LLHR) sulfides: The Harnas gold deposit, southwest Sweden, records continental-scale tectonic events: Economic Geology, v. 95, p. 1657-1671.

Stern, R.A., and Amelin, Y., 2003, Assessment of errors in SIMS zircon U–Pb geochronology using a natural zircon standard and NIST SRM 610 glass: Chemical Geology, v. 197, p. 111-142.

Sun, S.S., and McDonough, W.S., 1989, Chemical and isotopic systematics of oceanic basalts:

implications for mantle composition and processes: Geological Society, London, Special Publications, v. 42, p. 313-345.

Sun, W., Zhang, H., Ling, M.X., Ding, X., Chung, S.L., Zhou, J., Yang, X.Y., and Fan, W., 2011, The genetic association of adakites and Cu-Au ore deposits: International Geology Review, v. 53, p. 691-703.

Voudouris, P., 2011, Conditions of formation of the Mavrokoryfi high-sulfidation epithermal Cu-Ag-Au-Te mineralization (Petrota Graben, NE Greece): Mineralogy and Petrology, v. 101, p. 97-113.

Wan, B., Hegner, E., Zhang, L., Rocholl, A., Chen, Z., Wu, H., and Chen, F., 2009, Rb-Sr geochronology of chalcopyrite from the Chehugou porphyry Mo-Cu deposit (Northeast China) and geochemical constraints on the origin of hosting granites: Economic Geology, v. 104, p. 351-363.

Wang, C., 2015, Lead-zinc polymetallic metallogenic series and prospecting direction of Huangganglang-ganzhuermiao metallogenic belt, Inner Mongolia: Ph.D. thesis, Changchun, China, Jilin University, 165 p. (in Chinese with English abstract).

Wang, F., 2017, Magmatism and Ag-polymetallic mineralization in Shuangjianzishan deposit and its periphery, Inner Mongolia: Ph.D. thesis, Wuhan, China, China University of Geosciences, 176 p. (in Chinese with English abstract).

Wang, F., Bagas, L., Jiang, S., and Liu, Y., 2017, Geological, geochemical, and geochronological characteristics of Weilasituo Sn-polymetal deposit, Inner Mongolia, China: Ore Geology Reviews, v. 80, p. 1206-1229.

Wang, F., Sun, H., Pei, R., Liu, Y., Liu, C., and Jiang, S., 2016, The geologic features and genesis of Shuangjianzishan silver-polymetallic deposit, Balinzuo Qi, Inner Mongolia: Geological Review, v. 62, p. 1241-1256 (in Chinese with English abstract).

Wang, F., Zhou, X.H., Zhang, L.C., Ying, J.F., Zhang, Y.T., and Wu, F.Y., 2006, Timing of volcanism succession of the Great Xing'an Range, northeastern Asia, and its tectonic significance: Earth Planetary Science Letters, v. 251, p. 179-198.

Wang, J., 2009, Chronology and geochemistry of granitoid for the Weilasituo copper polymetal deposit in Inner Mongolia: Master thesis, China University of Geosciences Beijing, Beijing, China, 68 p. (in Chinese with English abstract).

Wang, J.B., Wang, Y.W., Wang, L.J., and Uemoto, T., 2001, Tin-polymetallic mineralization in the southern part of the Da Hinggan Mountains, China: Resource Geology, v. 51, p. 283-291.

Wang, T., Guo, L., Zheng, Y.D., Donskaya, T., Gladkochub, D., Zeng, L.S., Li, J.B., Wang, Y.B., and

Mazukabzov, A., 2012, Timing and processes of late Mesozoic mid-lower-crustal extension in continental NE Asia and implications for the tectonic setting of the destruction of the North China Craton: mainly constrained by zircon U–Pb ages from metamorphic core complexes: Lithos, v. 154, p. 315-345.

Wang, X.D., 2017, Magmatism and mineralization of Ag-Pb-Zn polymetallic deposits in the Lindong district, Inner Mongolia: Ph.D. thesis, Wuhan, China, China University of Geosciences, 175 p. (in Chinese with English abstract).

Wei, C.S., Zhao, Z.F., and Spicuzza, M.J., 2008, Zircon oxygen isotopic constraint on the sources of late Mesozoic A-type granites in eastern China: Chemical Geology, v. 250, p. 1-15.

Wiedenbeck, M., Alle, P., Corfu, F., Griffin, W.L., Meier, M., Oberli, F., Von Quadt, A., Roddick, J.C., and Spiegel, W., 1995, Three natural zircon standards for U-Th-Pb, Lu-Hf, trace element and REE analyses: Geostandards Newsletter, v. 19, p. 1-23.

Wilde, S.A., 2015, Final amalgamation of the Central Asian Orogenic Belt in NE China: Paleo-Asian Ocean closure versus Paleo-Pacific plate subduction—A review of the evidence: Tectonophysics, v. 662, p. 345-362.

Wilkinson, J.J., 2013, Triggers for the formation of porphyry ore deposits in magmatic arcs: Nature Geoscience, v. 6, p. 917.

Williams-Jones, A.E., and Heinrich, C.A., 2005, 100th Anniversary special paper: Vapor transport of metals and the formation of magmatic-hydrothermal ore deposits: Economic Geology, v. 100, p. 1287-1312.

Williams-Jones, A.E., and Migdisov, A.A., 2014, Experimental constraints on the transport and deposition of metals in ore-forming hydrothermal systems: Society of Economic Geologists, v. 18, p. 77-96.

Wood, S.A., 1998, Calculation of activity-activity and logfO_2-pH diagrams: Reviews in Economic Geology, v. 10, p. 81-96.

Wu, F.Y., Lin, J.Q., Wilde, S.A., Zhang, X.O., and Yang, J.H., 2005, Nature and significance of the Early Cretaceous giant igneous event in eastern China: Earth and Planetary Science Letters, v. 233, p. 103-119.

Wu, F.Y., Sun, D.Y., Ge, W.C., Zhang, Y.B., Grant, M.L., Wilde, S.A., and Jahn, B.M., 2011, Geochronology of the Phanerozoic granitoids in northeastern China: Journal of Asian Earth Sciences, v. 41, p. 1-30.

Wu, F.Y., Sun, D.Y., Li, H.M., Jahn, B.M., and Wilde, S.A., 2002, A-type granites in northeastern China: age and geochemical constraints on their petrogenesis: Chemical Geology, v. 187, p. 143-173.

Wu, G., 2014, Research of silver mineralization in central-southern segment of the Great Xing'an Range - A case study of the Shuangjianzishan silver deposit, Inner Mongolia: Ph.D. thesis, University of Chinese Academy of Sciences, Beijing, China, 136 p. (in Chinese with English abstract).

Wu, G., Liu, J., Zeng, Q., Liu, M., Sun, H., Yin, Z., and Yin, X., 2014, Occurrences of silver in the Shuangjianzishan Pb-Zn-Ag deposit and its implications for mineral processing: Earth Science Frontiers, v. 21, p. 105-115 (in Chinese with English abstract).

Wu, G., Liu, J., Zeng, Q., Sun, H., and Liu, M., 2013, The metallogenic age of Shuangjianzishan Ag–Pb–Zn deposit of Greate Hinggan Range, Inner Mongolia: Acta Mineralogica Sinica, v. 33, p. 619 (in Chinese).

Wu, X.L., Mao, J.W., Zhou, Z.H., and Ouyang, H.G., 2012, H-O-S-Pb isotopic components of the Budunhua Cu deposit in the middle-south part of the Da Hinggan Mountains and their implications for the ore-forming process: Geology in China, v. 39, p. 1812-1829 (in Chinese with English abstract).

Xiao, W.J., Zhang, L.C., Qin, K.Z., Sun, S., and Li, J.L., 2004, Paleozoic accretionary and collisional tectonics of the eastern Tianshan China: Implication for the continental growth of central Asia: American Journal of Science, v. 304, p. 370-395.

Yao, M.J., Liu, J.J., Zhai, D.G., and Wang, J.P., 2012, Sulfur and lead isotopic compositions of the polymetallic deposits in the southern Great Xing'an Range: some implications for metal sources: Journal of Jilin University (Earth Science Edition), v. 42, p. 362-373 (in Chinese with English abstract).

Yuan, H., Yin, C., Liu, X., Chen, K., Bao, Z., Zong, C., Dai, M., Lai, S., Wang, R., and Jiang, S., 2015, High precision in-situ Pb isotopic analysis of sulfide minerals by femtosecond laser ablation multi-collector inductively coupled plasma mass spectrometry: Science China Earth Sciences, v. 58, p. 1713-1721.

Zeng, Q., Liu, J., Chu, S., Guo, Y., Gao, S., Guo, L., and Zhai, Y., 2016, Poly-metal mineralization and exploration potential in southern segament of the Da Hinggan Mountains: Journal of Jilin University (Earth Science Edition), v. 46, p. 1100-1123 (in Chinese with English abstract).

Zeng, Q., Qin, K., Liu, J., Li, G., Zhai, M., Chu, S., and Guo, Y., 2015, Porphyry molybdenum deposits in the Tianshan–Xingmeng orogenic belt, northern China: International Journal of Earth Sciences, v. 104, p. 991-1023.

Zeng, Q.D., Liu, J.M., Zhang, Z.L., Chen, W.J., and Zhang, W.Q., 2011, Geology geochronology of the Xilamulun molybdenum metallogenic belt in eastern Inner Mongolia, China: International Journal of Earth Sciences, v. 100, p. 1791-1809.

Zeng, Q.D., Liu, J.M., Zhang, Z.L., Jia, C.S., Yu, C.M., Ye, J., and Liu, H.T., 2009, Geology and lead-isotope study of the Baiyinnuoer Zn-Pb-Ag deposit, south segment of the Da Hinggan Mountains, Northeastern China: Resource Geology, v. 59, p. 170-180.

Zhai, D., Bindi, L., Voudouris, P.C., Liu, J., Tombros, S.F., and Li, K., 2019c, Discovery of Se-rich canfieldite, $Ag_8Sn(S, Se)_6$, from the Shuangjianzishan Ag-Pb-Zn deposit, NE China: A multimethodic chemical and structural study: Mineralogical Magazine, v. 83, p. 419-426.

Zhai, D., Williams-Jones, A.E., Liu, J., Selby, D., Li, C., Huang, X.W., Qi, L., and Guo, D., 2019b, Evaluating the use of the molybdenite Re-Os chronometer in dating gold mineralization: Evidence from the Haigou deposit, NE China: Economic Geology (in press).

Zhai, D., Liu, J., Cook, N.J., Wang, X., Yang, Y., Zhang, A., and Jiao, Y., 2019a, Mineralogical, textural, sulfur and lead isotope constraints on the origin of Ag-Pb-Zn mineralization at Bianjiadayuan, Inner Mongolia, NE China: Mineralium Deposita, v. 54, p. 47-66.

Zhai, D., Williams-Jones, A.E., Liu, J., Tombros, S.F., Cook, N.J., 2018a, Mineralogical, fluid inclusion and multiple isotope (H-O-S-Pb) constraints on the genesis of the Sandaowanzi epithermal Au-Ag-Te deposit, NE China: Economic Geology, v. 113, p. 1359-1382.

Zhai, D., Liu, J., Li, J., Zhang, M., Li, B., Fu, X., Jiang, H., Ma, L., and Qi, L., 2016, Geochronological study of Weilasituo porphyry type Sn deposit in Inner Mongolia and its geological significance: Mineral Deposits, v. 35, p. 1011-1022 (in Chinese with English abstract).

Zhai, D., Liu, J., Ripley, E.M., and Wang, J., 2015, Geochronological and He–Ar–S isotopic constraints on the origin of the Sandaowanzi gold-telluride deposit, northeastern China: Lithos, v. 212, p. 338-352.

Zhai, D., Liu, J., Tombros, S., and Williams-Jones, A.E., 2018b, The genesis of the Hashitu porphyry molybdenum deposit, Inner Mongolia, NE China: constraints from mineralogical, fluid inclusion, and multiple isotope (H, O, S, Mo, Pb) studies: Mineralium Deposita, v. 53, p. 377-397.

Zhai, D., Liu, J., Wang, J., Yang, Y., Zhang, H., Wang, X., Zhang, Q., Wang, G., and Liu, Z., 2014a, Zircon U-Pb and molybdenite Re-Os geochronology, and whole-rock geochemistry of the Hashitu molybdenum deposit and host granitoids, Inner Mongolia, NE China: Journal of Asian Earth Sciences, v. 79, p. 144-160.

Zhai, D., Liu, J., Zhang, A., and Sun, Y., 2017, U-Pb, Re-Os and $^{40}Ar/^{39}Ar$ geochronology of porphyry Sn ± Cu ± Mo and polymetallic (Ag-Pb-Zn-Cu) vein mineralization at Bianjiadayuan, Inner Mongolia, NE China: Implications for discrete mineralization events: Economic Geology, v. 112, p. 2041-2059.

Zhai, D., Liu, J., Zhang, H., Tombros, S., and Zhang, A., 2018c, A magmatic-hydrothermal origin for Ag-Pb-Zn vein formation at the Bianjiadayuan deposit, Inner Mongolia, NE China: Evidences from fluid inclusion, stable (C-H-O) and noble gas isotope studies: Ore Geology Reviews, v. 101, p. 1-16.

Zhai, D., Liu, J., Zhang, H., Yao, M., Wang, J., and Yang, Y., 2014b, S-Pb isotopic geochemistry, U-Pb and

Re-Os geochronology of the Huanggangliang Fe-Sn deposit, Inner Mongolia, NE China: Ore Geology Reviews, v. 59, p. 109-122.

Zhang, F.Q., Chen, H.L., Yu, X., Dong, C.W., Yang, S.F., Pang, Y.M., and Batt, G.E., 2011, Early Cretaceous volcanism in the northern Songliao Basin, NE China, and its geodynamic implication: Gondwana Research, v. 19, p. 163-176.

Zhang, J.H., Gao, S., Ge, W.C., Wu, F.Y., Yang, J.H., Wilde, S.A., and Li, M., 2010, Geochronology of the Mesozoic volcanic rocks in the Great Xing'an Range, northeastern China: implications for subduction-induced delamination: Chemical Geology, v. 276, p. 144-165.

Zhang, L.C., Zhou, X.H., Ying, J.F., Wang, F., Guo, F., Wan, B., and Chen, Z.G., 2008, Geochemistry and Sr-Nd-Pb-Hf isotopes of Early Cretaceous basalts from the Great Xinggan Range, NE China: Implications for their origin and mantle source characteristics: Chemical Geology, v. 256, p. 12-23.

Zhang, L.G., Liu, J.X., and Wang, K.F., 1995, Block geology of eastern Asia lithosphere: Isotope geochemistry and dynamics of upper mantle, basement and granite. Beijing: Science Press, 252 p. (in Chinese with English abstract).

Zhang, Z., 2018, Geological and geochemical characteristics and metallogenic mechanism of the Shuangjianzishan Ag-polymetallic deposit, Inner Mongolia, Master thesis, Beijing, China, China University of Geosciences Beijing, 64 p. (in Chinese with English abstract).

Zhou, J.B., Wilde, S.A., Zhao, G.C., and Han, J., 2018, Nature and assembly of microcontinental blocks within the Paleo-Asian Ocean: Earth-Science Reviews, v. 186, p. 76-93.

Zhou, Z.H., Ouyang, H.G., Wu, X.L., Liu, J., and Che, H.W., 2014, Geochronology and geochemistry study of the biotite granite from the Daolundaba Cu-W polymetallic deposit in the Inner Mogolia and its geological significance: Acta Petrologica Sinica, v. 30, p. 79-94 (in Chinese with English abstract).

Zhu, X.Y., Zhang, Z.H., Fu, X., Li, B.Y., Wang, Y.L., Jiao, S.T., and Sun, Y.L., 2016, Geological and geochemical characteristics of the Weilasito Sn-Zn deposit, Inner Mongolia: Geology in China, v. 43, p. 188-208 (in Chinese with English abstract).

Figure Captions

Figure 1 (A) A tectonic map of the Central Asian Orogenic Belt (based on Jahn et al., 2000); (B) A geological map of the Great Hinggan Range (GHR) in NE China showing the distribution of the Mesozoic granites and volcanic rocks (modified from Qi et al., 2005); (C) A geological map of the southern GHR

showing the locations and ages of major ore deposits (modified from Zhai et al., 2017).

Figure 2 (A) A geological map of the Shuangjianzishan ore district (based on Wu et al., 2014); (B) A vertical section through the ore deposit (modified from Wang, 2015).

Figure 3 Core logs of two drill holes showing the distribution of granite porphyry and Mo mineralization (A), and a diorite dike and Ag-Pb-Zn mineralization (B). Also shown are the locations of samples used in geochronological analyses. Abbreviations: Ab-albite; Mo-molybdenite; Cal-calcite; Qtz-quartz.

Figure 4 (A) Oxidized mineralized veins hosted in slate near the erosional surface; (B) Major and parallel Ag-Pb-Zn-quartz veins hosted by slate associated with an alteration assemblage of chlorite-sericite-quartz; (C) Early formed pyrite veinlets within slate enclosed as breccias in subsequent massive Ag-Pb-Zn quartz-calcite veins; (D) Early quartz-pyrite veins crosscut by Ag-Pb-Zn mineralized quartz-calcite veins, and a late stage quartz vein crosscutting the Ag-Pb-Zn mineralized veins; (E) Massive Ag-Pb-Zn ore with a very high Ag grade (>32,000 g/t) from a major mineralized vein; (F) Massive sulfide ore comprising galena, sphalerite and pyrite; (G) Slate as breccia fragments cemented by quartz, calcite and sulfides. Abbreviations: Cal-calcite; Chl-chlorite; Gn-galena; Py-pyrite; Q-Quaternary gravel; Qtz-quartz; Sec-sericite; Sp-sphalerite.

Figure 5 The paragenetic sequence for the Shuangjianzishan Ag-Pb-Zn mineralization.

Figure 6 Photomicrographs of ore textures involving silver-bearing minerals, and mineral assemblages from the Shuangjianzishan deposit. (A) Galena and sphalerite replaced by argentite and canfieldite coexisting with sericite and quartz (BSE); (B) Early pyrite surrounded by later chalcopyrite, which was replaced by argentite and canfieldite (reflected light); (C) Canfieldite intergrown with freibergite that replaced sphalerite and galena (reflected light); (D) Galena and chalcopyrite associated with freibergite and canfieldite (reflected light); (E) Argentite after galena, sphalerite and chalcopyrite (BSE); (F) Late argentite as veins cutting galena (reflected light); (G) Ellipsoidal inclusions of freibergite, pyrargyrite and pyrrhotite within galena (BSE); (H) Coexisting stephanite and freibergite that replaced galena and sphalerite (reflected light); (I) Polybasite associated with quartz and sericite after galena (BSE).

Abbreviations: Arg-argentite; Caf-canfieldite; Ccp-chalcopyrite; Frb-freibergite; Gn-galena; Po-pyrrhotite; Pol-polybasite; Py-pyrite; Pyr-pyrargyrite; Qtz-quartz; Sec-sericite; Sp-sphalerite; Ste-stephanite.

Figure 7 Reflected light (A) and EPM element maps (B-I) of canfieldite and argentite. Abbreviations: Arg-argentite; Caf-canfieldite; Cas-cassiterite; Ccp-chalcopyrite; Sp-sphalerite.

Figure 8 Locations of in situ spot sulfur isotopic analyses of sulfide and sulfosalt minerals and corresponding $\delta^{34}S$ values. (A): Galena and sphalerite; (B): A single galena crystal; (C): Freibergite and galena; (D): Pyrargyrite, canfieldite and galena. Abbreviations: Caf-canfieldite; Frb-freibergite; Gn-galena; Ccp-chalcopyrite; Pyr-pyrargyrite; Qtz-quartz; Sp-sphalerite.

Figure 9 (A) A histogram of $\delta^{34}S$ values for various ore minerals from the different ore stages; (B) $\delta^{34}S$ values for ore minerals versus depth.

Figure 10 Binary plots of $^{206}Pb/^{204}Pb$ vs. $^{207}Pb/^{204}Pb$ (A) and $^{206}Pb/^{204}Pb$ vs. $^{208}Pb/^{204}Pb$ (B) for ore minerals from the Shuangjianzishan deposit.

Figure 11 Zircon U-Pb ages for igneous rocks from the Shuangjianzishan deposit. (A): Diorite dike; (B): Dacite; (C): Granite intrusion; (D): Coarse-grained granite porphyry; (E): Fine-grained granite porphyry.

Figure 12 Molar Ag/(Ag+Cu) and Zn/(Zn+Fe) plots for primary freibergite in the Shuangjianzishan deposit. The isotherms were calculated from Sack (2005). These isotherms terminate at low Zn/(Zn+Fe) and high Ag/(Ag+Cu) ratios because of saturation with respect to pyrrhotite (Po) (Balabin and Sack, 2000).

Figure 13 Lead isotope plots of the Shuangjianzishan ore minerals compared to local magmatic-hydrothermal deposits and various rock units. The Pb isotope data for local Mesozoic granite, andesite and basalt, Paleozoic granite, Permian slate, and sulfides from the nearby magmatic-hydrothermal deposits were taken from the literature (Zhang et al., 1995, 2008; Shen and Fu, 1999; Chu et al., 2001;

Cai et al., 2004; Wang, 2009; Zeng et al., 2009; Guo et al., 2010; Jiang et al., 2010; Shao et al., 2010; Yao et al., 2012; Wu et al., 2012; Zhai et al., 2014b, 2018b, 2019a). The Pb isotope ratios for the Shuangjianzishan deposit are similar to those of the local Mesozoic granite and adjacent ore deposits. (A): $^{206}Pb/^{204}Pb$ vs. $^{207}Pb/^{204}Pb$ plots; (B): $^{206}Pb/^{204}Pb$ vs. $^{208}Pb/^{204}Pb$ plots.

Figure 14 LogfO_2-pH diagrams showing stability relationships in the Fe-O-S system and alteration assemblages for Ag-Pb-Zn mineralization in the Shuangjianzishan deposit at 250 °C (A) and 200 °C (B) and 300 bars. The calculations assumed an aqueous fluid with a $\Sigma\alpha S$ value of 0.01 and a $\delta^{34}S_{\Sigma S}$ value of +0.5‰. The diagrams show the predominance boundaries of aqueous sulfur species (pink dashed), mineral stability in the Fe-O-S system (black solid), alteration equilibra (grey solid), and calcite dissolution (black dashed). The kaolinite–muscovite and K–feldspar–muscovite stability fields are for a solution with a K^+ activity of 0.001. The stability boundary for calcite is for ΣC = 1 m (based on Ohmoto, 1972). The sulfur isotope contours are indicated by blue lines. The grey area represents the approximate stability field for the ore minerals. Phase and predominance boundaries were constructed using the HCh software package (Shvarov, 2011). Abbreviations: Hem-hematite; Kfs-K-feldspar; Kln-kaolinite; Mag-magnetite; Mus-muscovite; Po-pyrrhotite; Py-pyrite .

Figure 15 (A) A chronology of magmatic and mineralization events in the Shuangjianzishan ore district; some of the data are from the literature (Wu, 2014; Cui, 2015; Liu, C., et al., 2016; Gu et al., 2017; Zhang, 2018). The uncertainty for all the data is 2σ; (B)-(D): Cartoons illustrating the sequence of magmatic and mineralizing events from ~252 to 132 Ma in the Shuangjianzishan ore district.

Appendix Data

Figure A1 A total alkali vs. silica diagram illustrating the classification of the magmatic rocks at Shuangjianzishan (after Middlemost, 1994). The alkaline/subalkaline boundary is from Irvine and Baragar (1971). Some of the petrochemical data are from Gu et al. (2017) and Zhang (2018).

Figure A2 Geochemical data for the magmatic rocks in the Shuangjianzishan ore district. (A)-(D): Harker diagrams of Al_2O_3, CaO, MgO and TiO_2 versus SiO_2; (E) A K_2O-SiO_2 diagram (Rickwood, 1989); (F) A A/NK-A/CNK diagram (Maniar and Piccoli, 1989).

Figure A3 Trace element diagrams for the granite porphyry and dacite. (A) Rare earth element profiles normalized to the CI chondrite of McDonough and Sun (1995); (B) Spider diagram of trace elements normalized to the primitive mantle composition of Sun and McDonough (1989).

Figure A4 A histogram of temperatures determined using sulfur isotope geothermometry.

Figure A5 Comparisons of the Pb isotope ratios obtained using in situ and conventional (mineral separates) analytical methods; the mineral separate data are from Wang, F. (2017). (A): $^{206}Pb/^{204}Pb$ versus $^{207}Pb/^{204}Pb$; (B): $^{206}Pb/^{204}Pb$ versus $^{208}Pb/^{204}Pb$.

Figure A6 Trace element tectonic discrimination diagrams. (A) Sr/Y versus Y (Defant and Drummond, 1993); (B) Y + Nb versus Rb (Pearce et al., 1984).

Table A1 Electron microprobe-determined compositions of sulfides and sulfosalts from the Shuangjianzishan Ag-Pb-Zn deposit (wt.%).

Table A2 LA-ICP-MS zircon U-Pb isotopic data for various igneous rocks from the Shuangjianzishan deposit.

Table A3 Lead isotope ratios for sulfides from ore deposits and a variety of rock units in the southern GRH region.

Figure 1

Click here to access/download;Figure;Fig 1 regional geol-revised.jpg

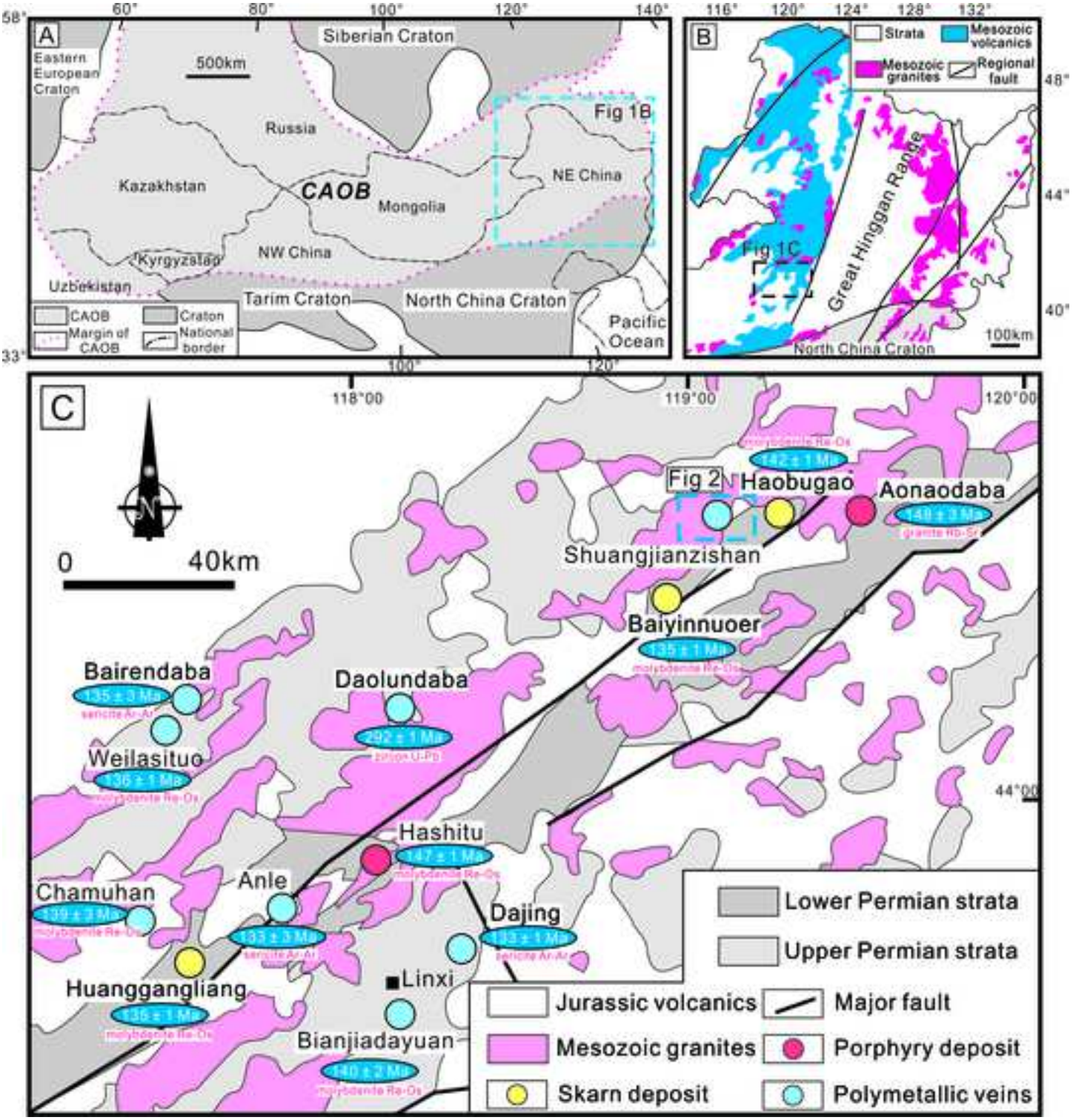

Figure 2

Click here to access/download;Figure;Fig 2 ore deposit geol-revised.jpg

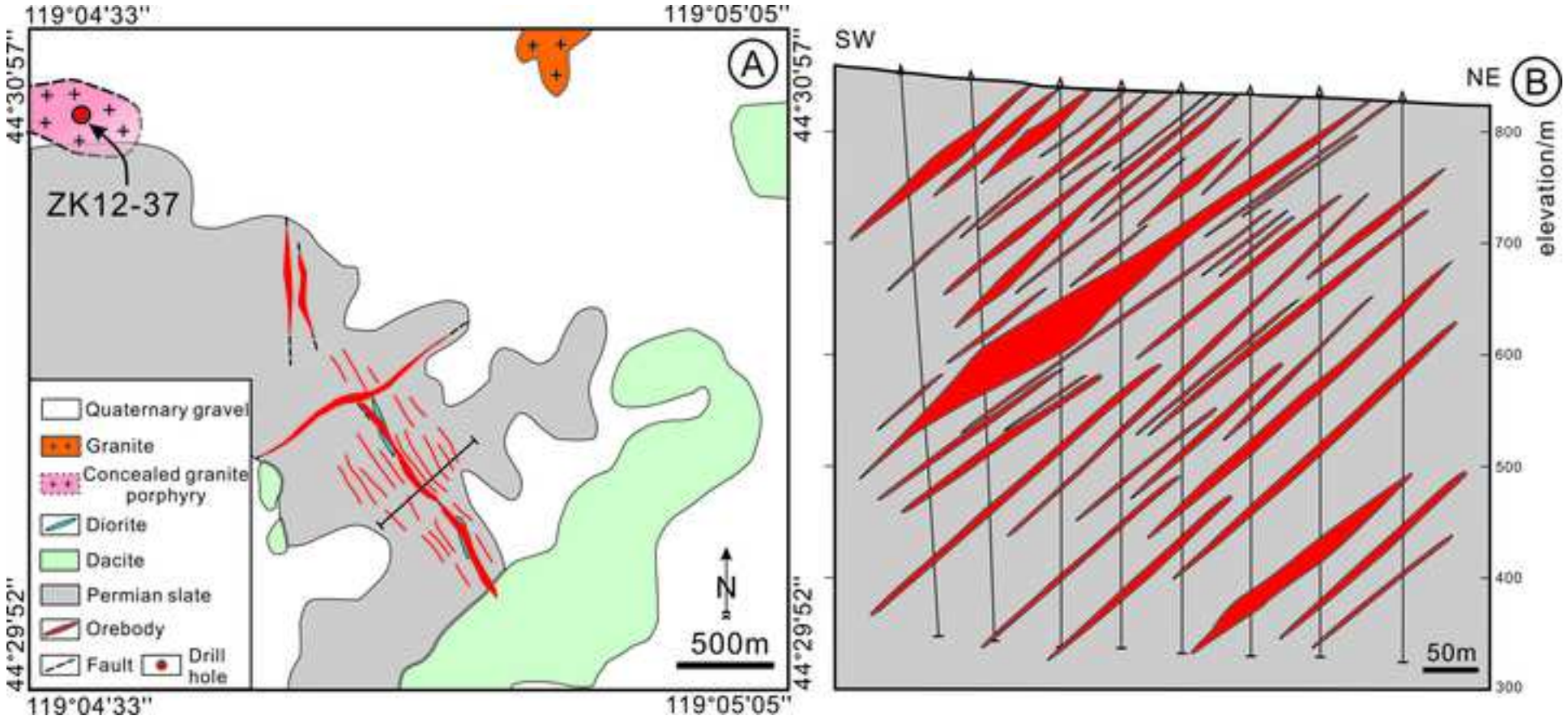

Figure 3

Click here to access/download;Figure;Fig 3 core logging-revised.jpg

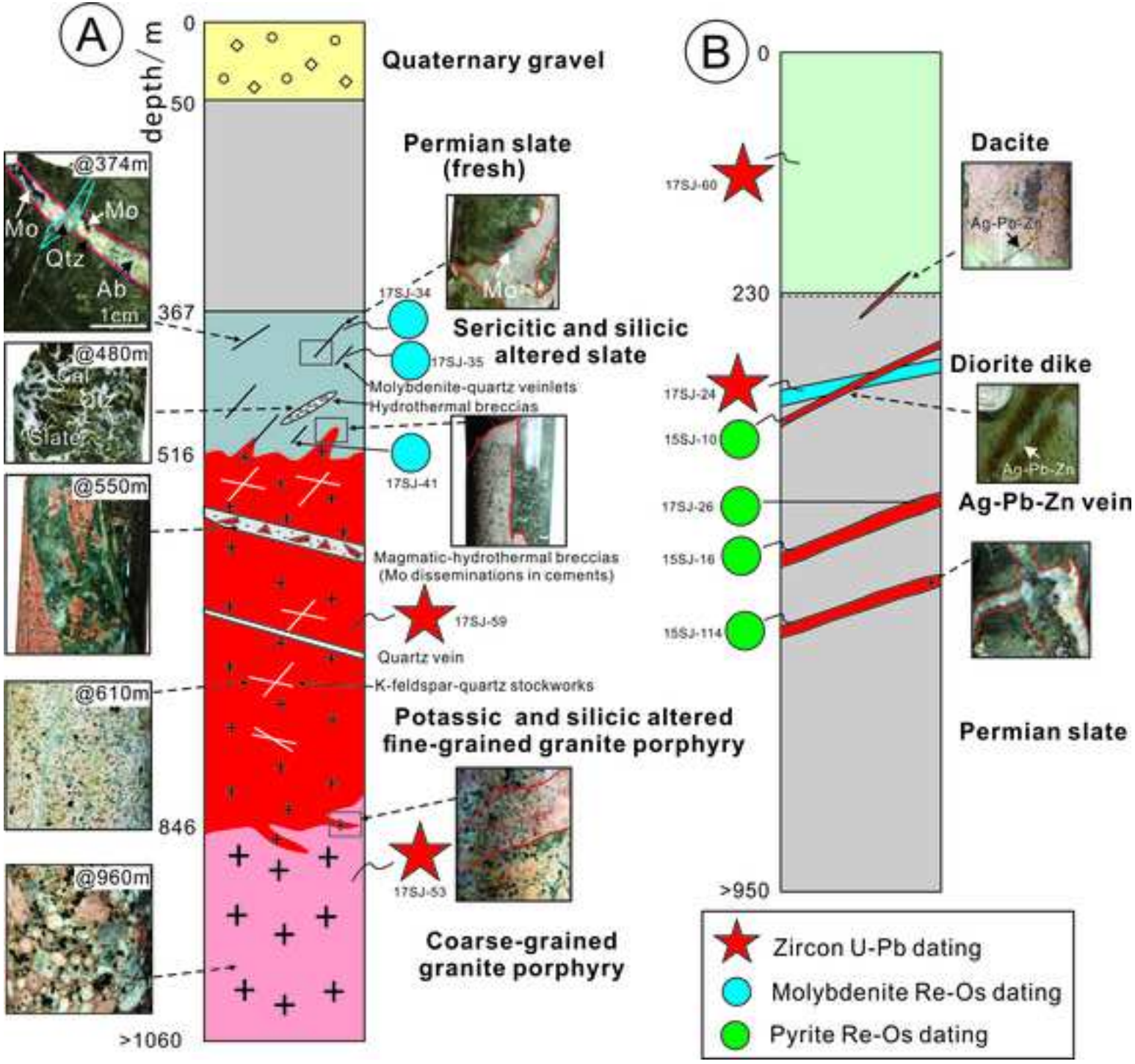

Figure 4

Click here to access/download;Figure;Fig 4 ore bodies-revised.jpg

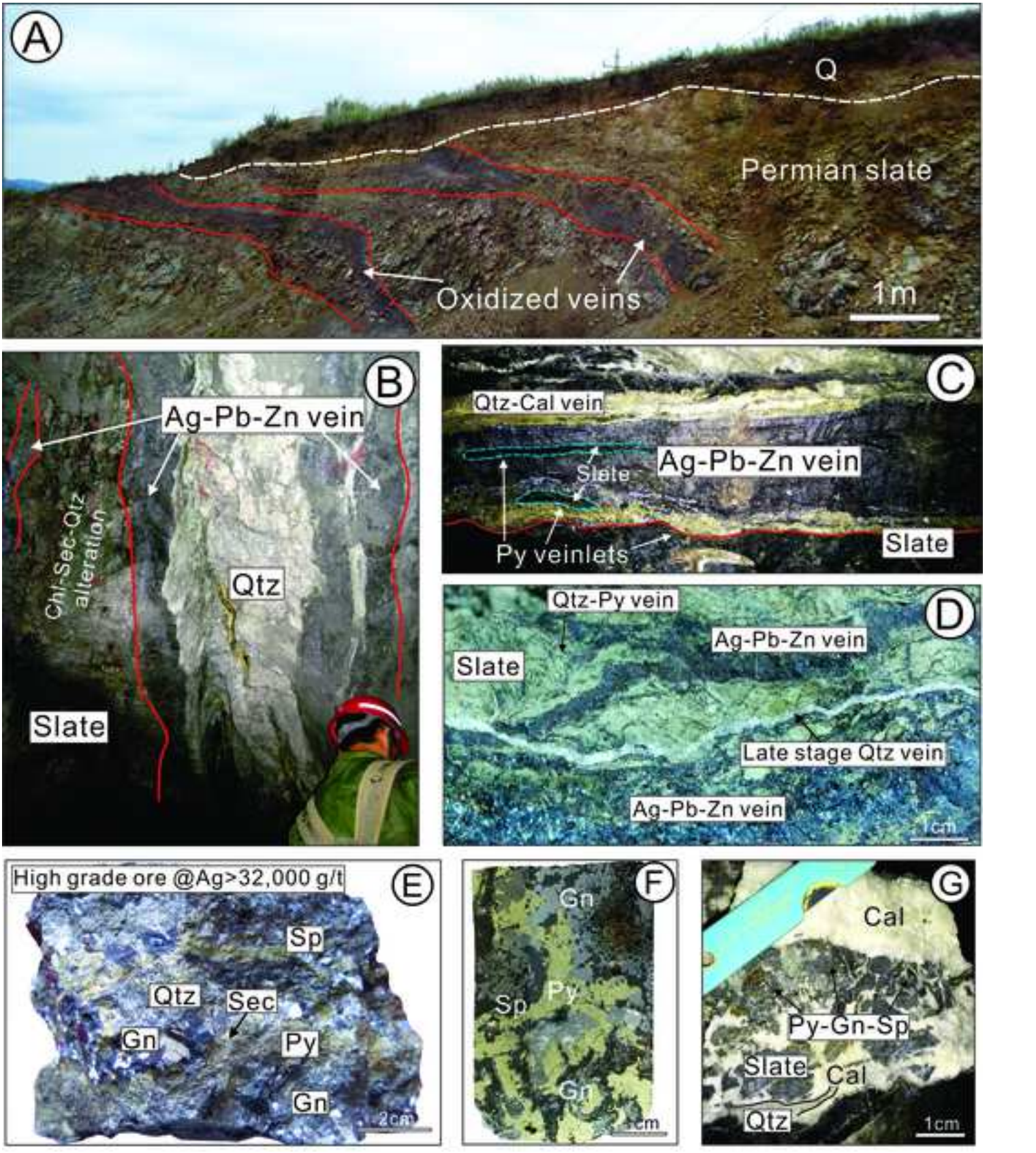

Figure 5

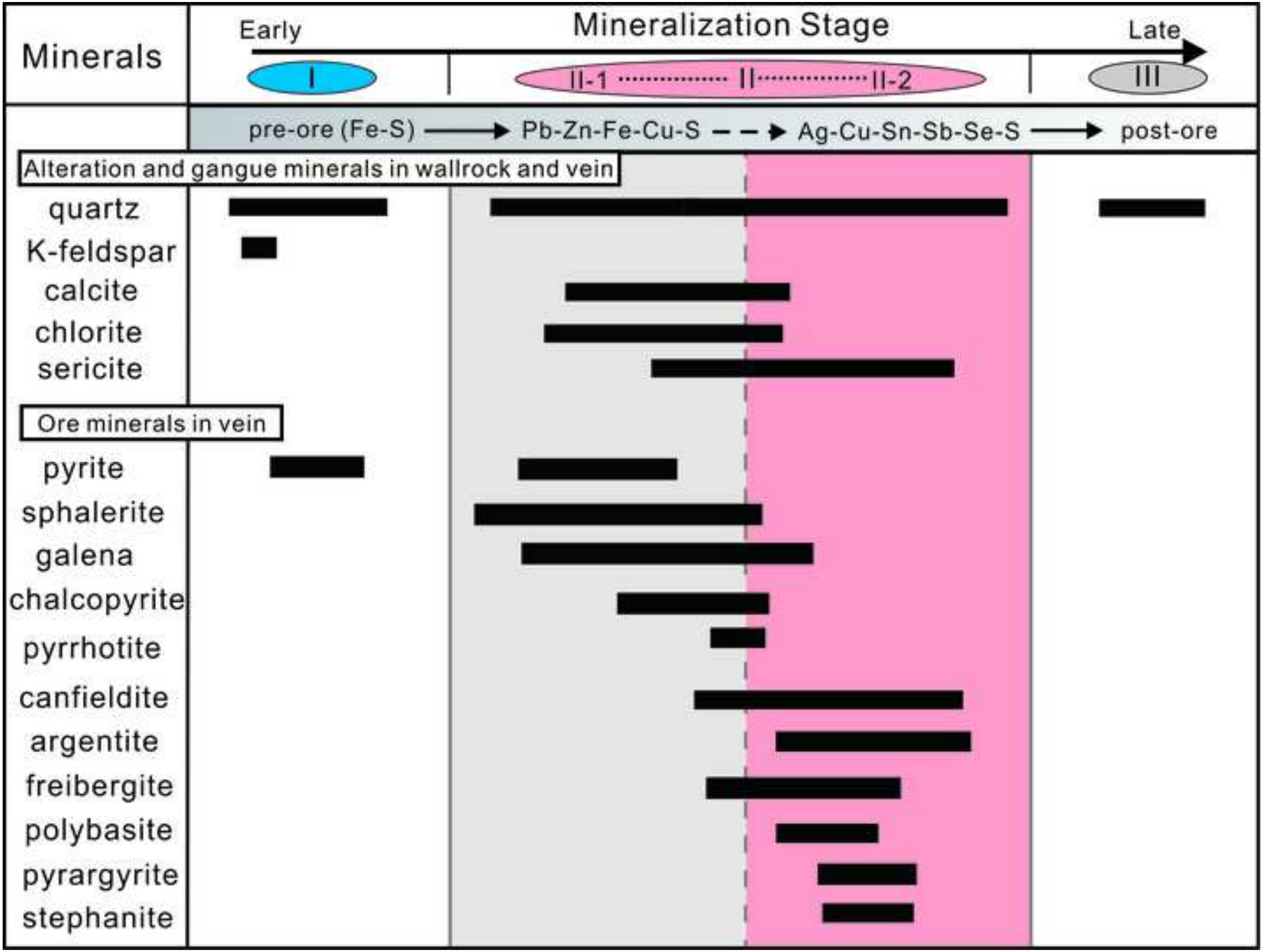

Figure 6

Click here to access/download;Figure;Fig 6 Ag minerals.jpg

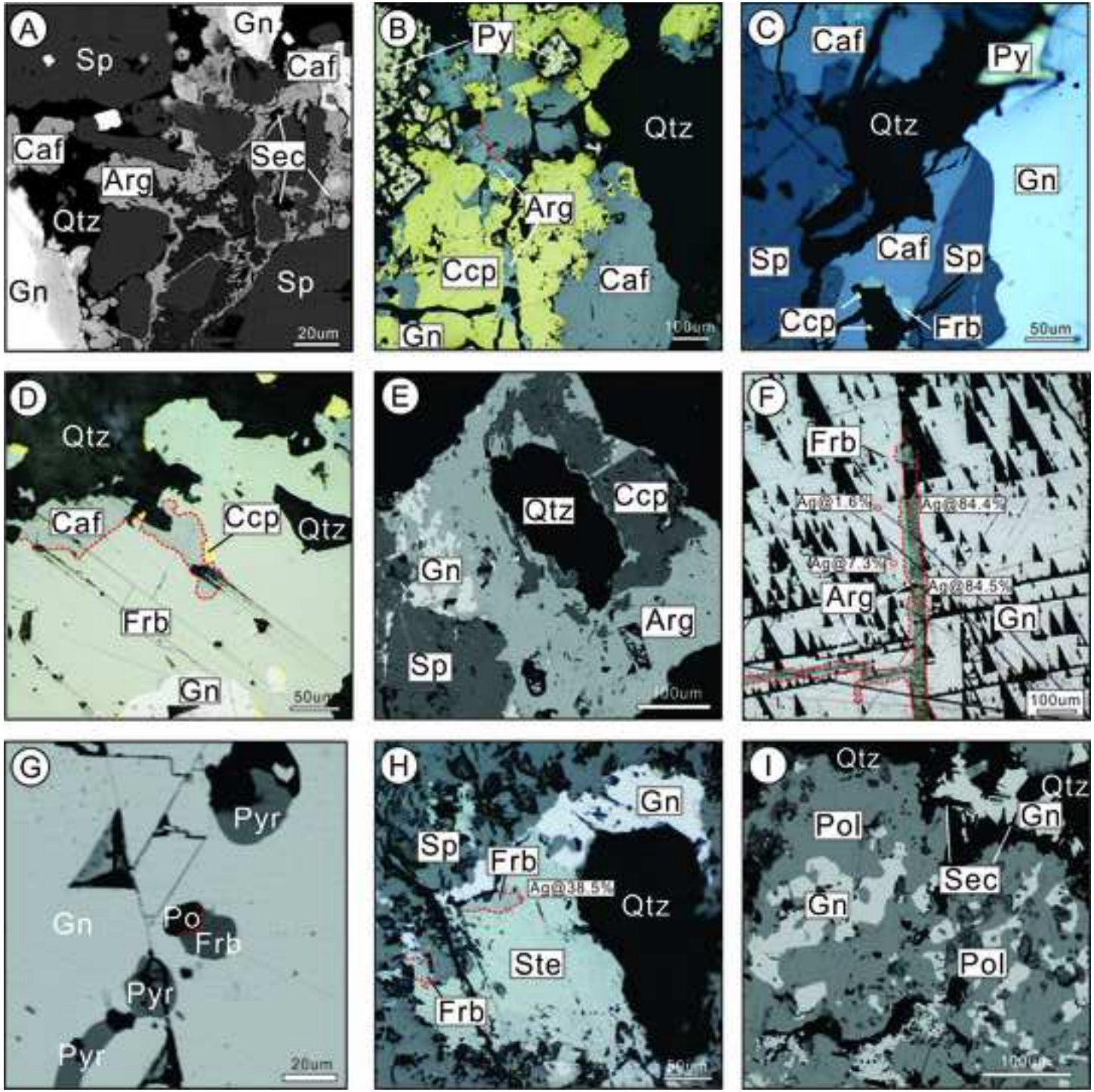

Figure 7

Click here to access/download;Figure;Fig 7 element mapping.jpg

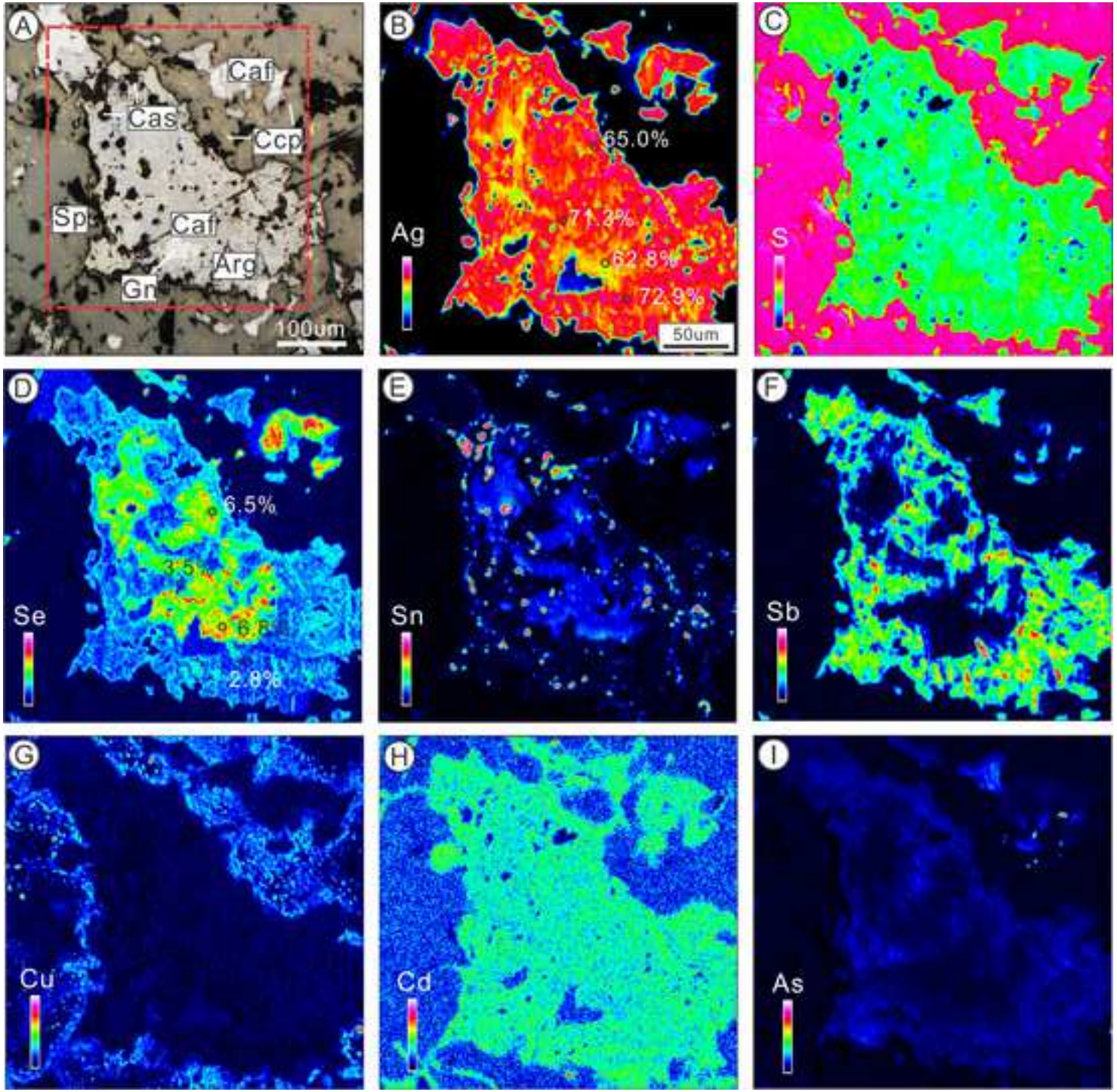

Figure 8

Click here to access/download;Figure;Fig 8 SJ in situ S isotope-revised.jpg

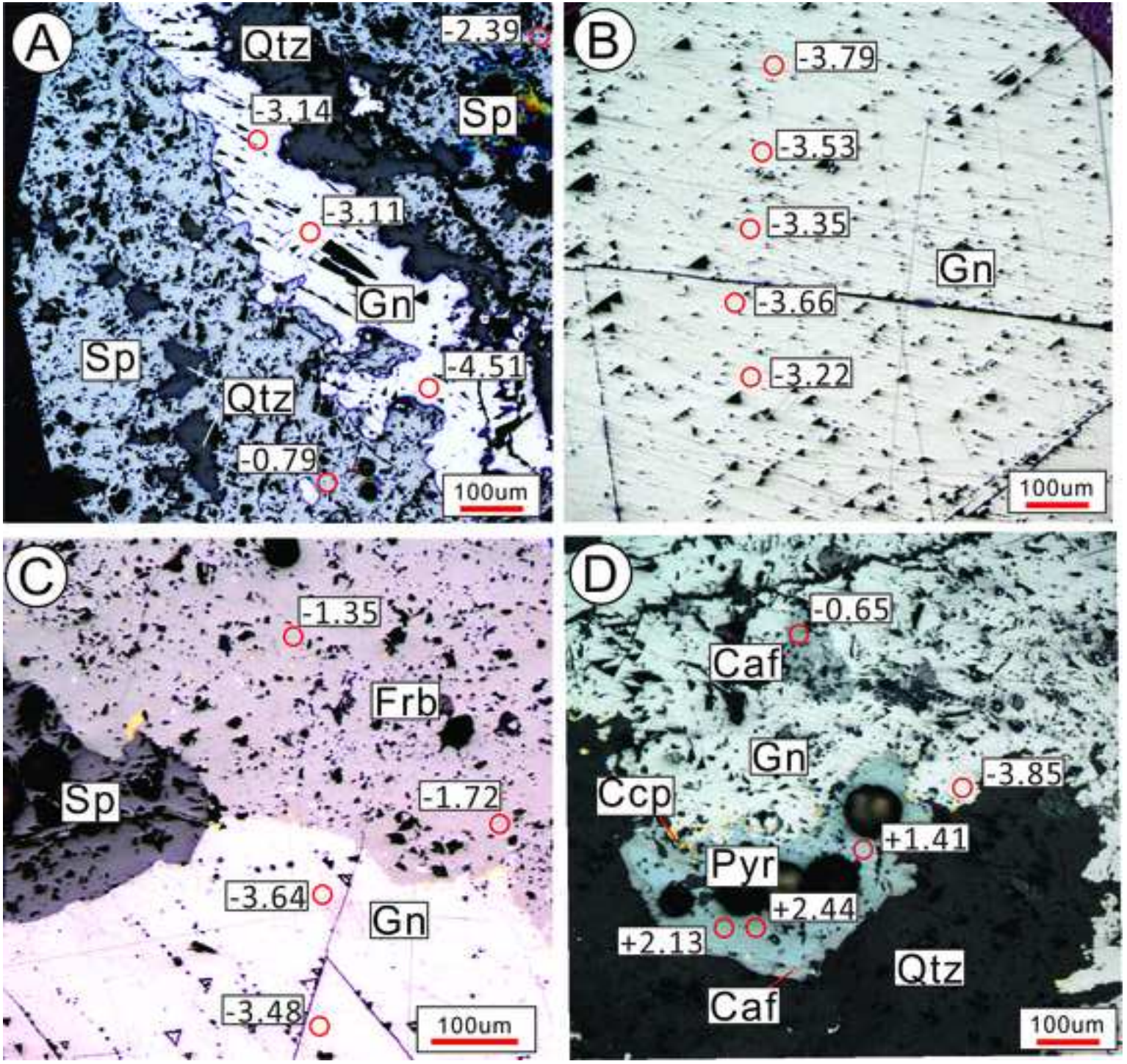

Figure 9

Click here to access/download;Figure;Fig 9 S hisgram.jpg

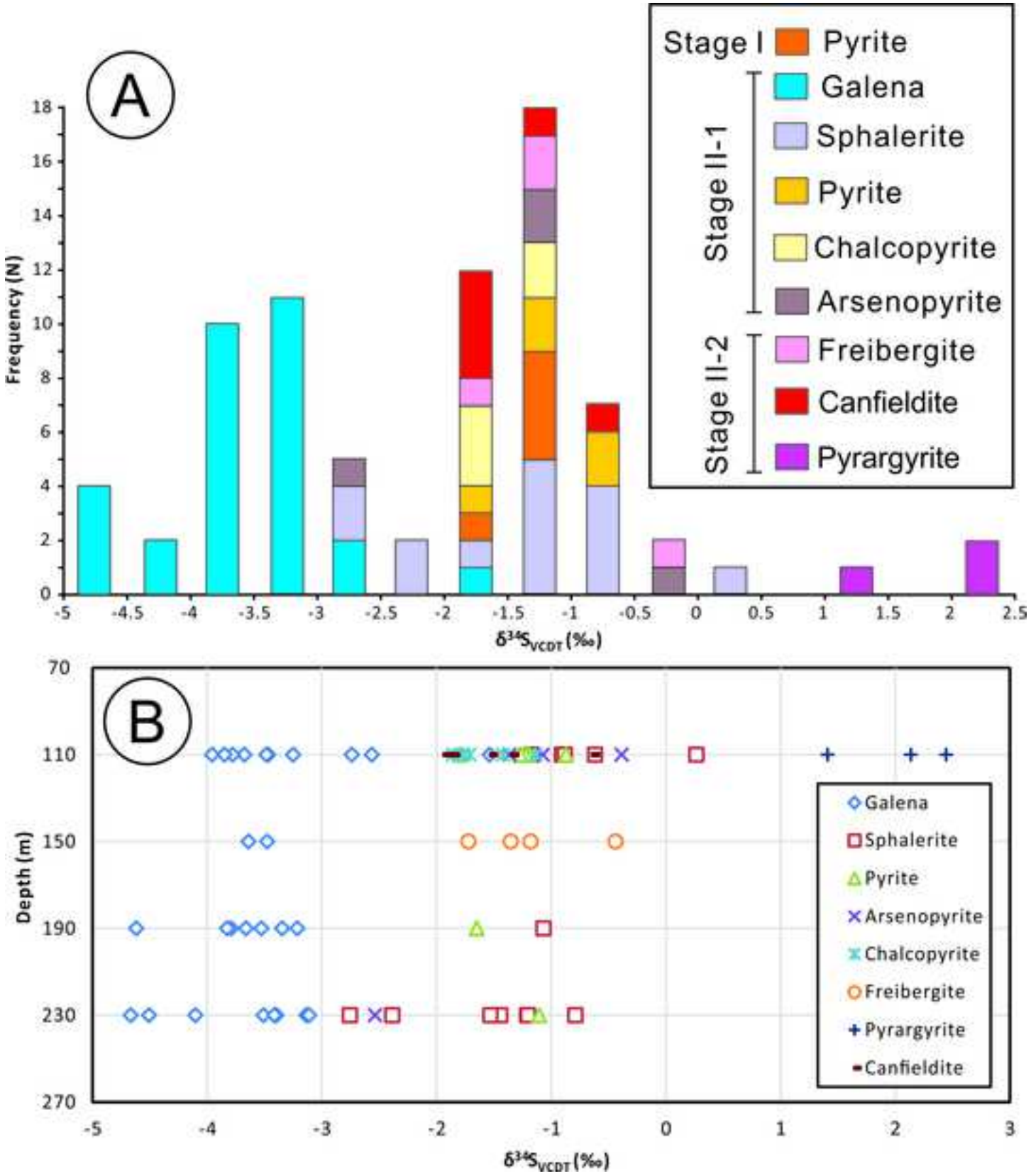

Figure 10

Click here to access/download;Figure;Fig 10 Pb isotopes by minerals.jpg

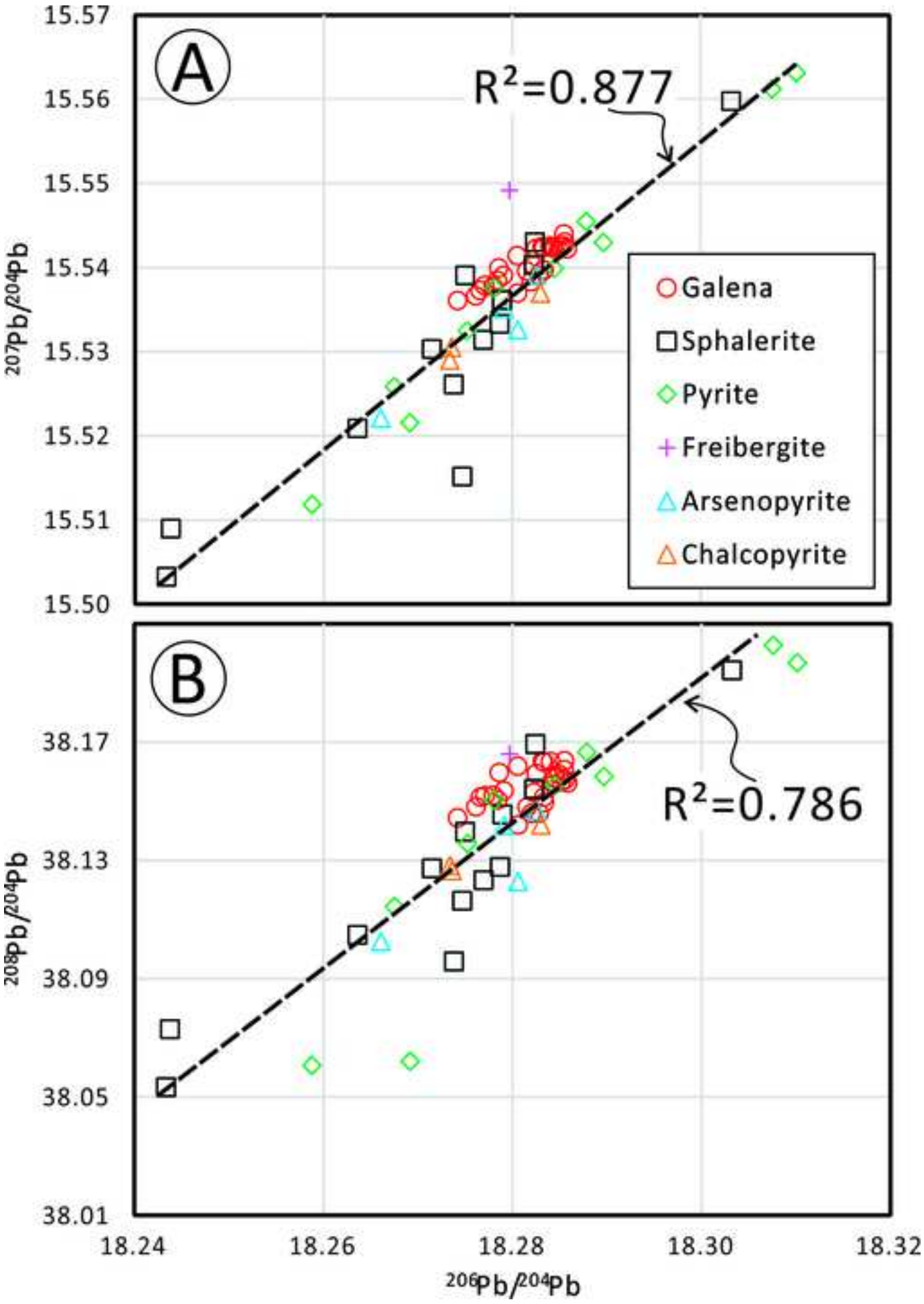

Figure 11

Click here to access/download;Figure;Fig 11 Zircon U-Pb age results-revised.jpg

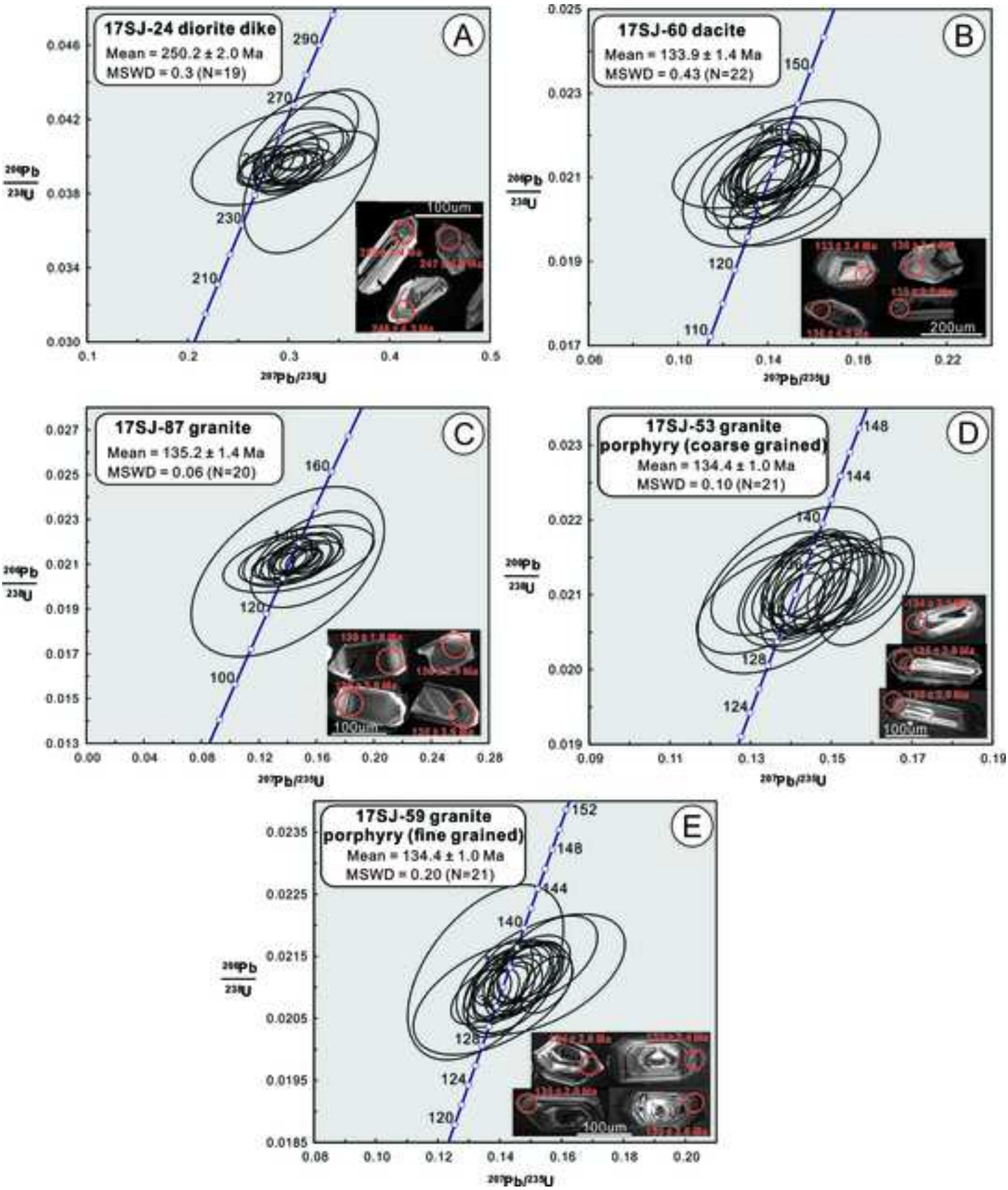

Figure 12

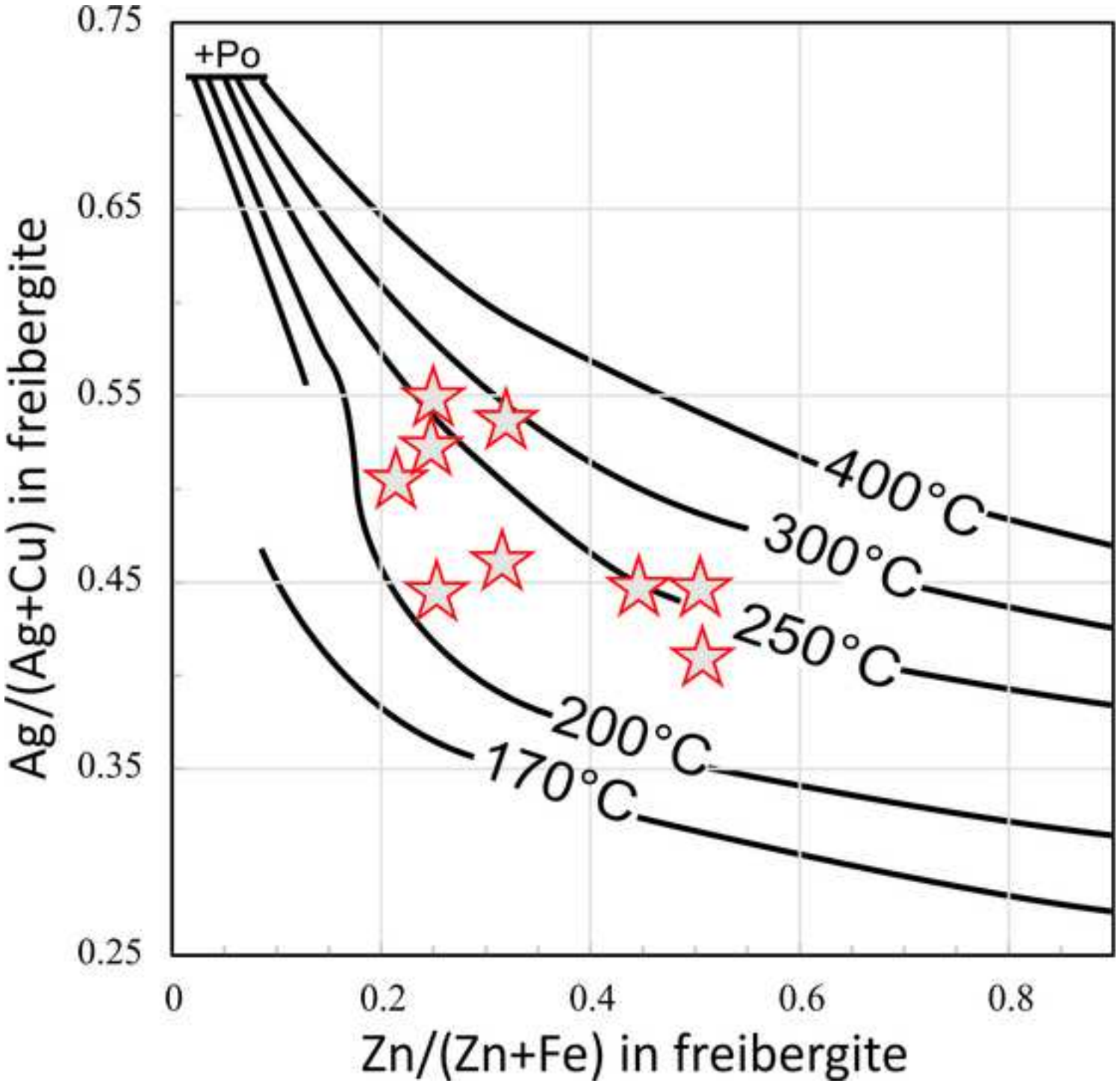

Figure 13

Click here to access/download;Figure;Fig 13 SJ Pb isotope-revised.jpg

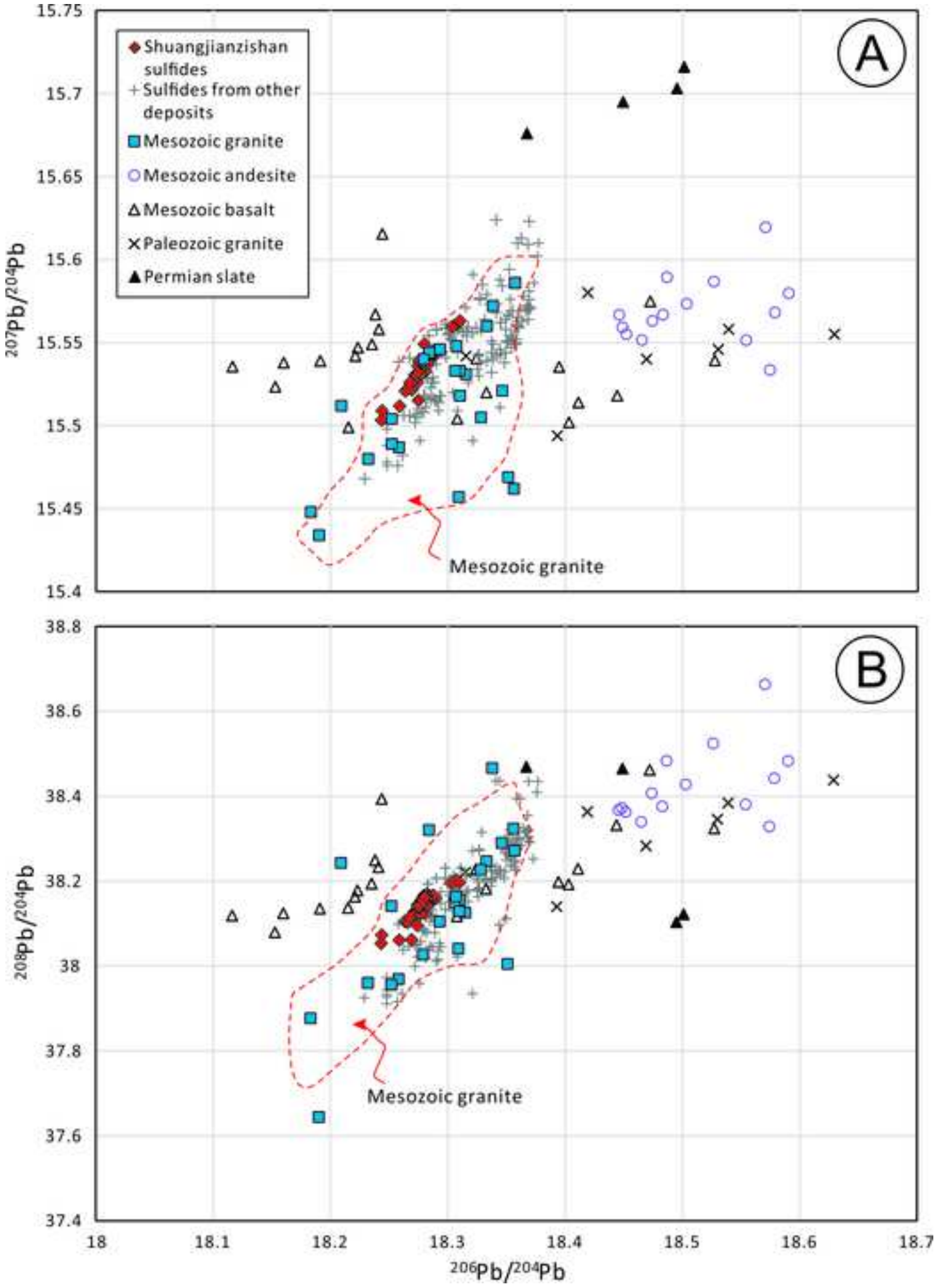

Figure 14

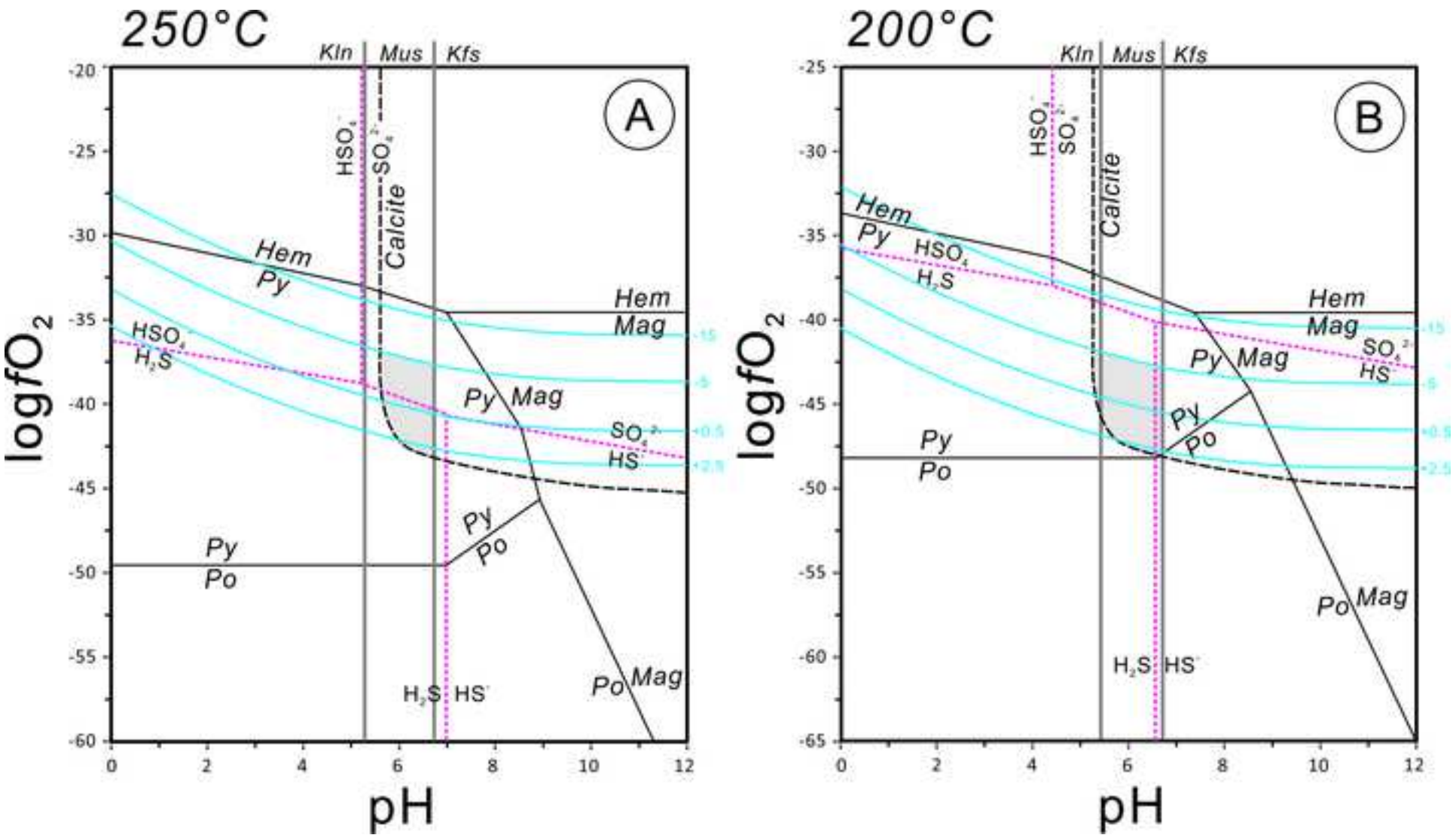

Figure 15

Click here to access/download;Figure;Fig 15 geochronological data summary-revised.jpg

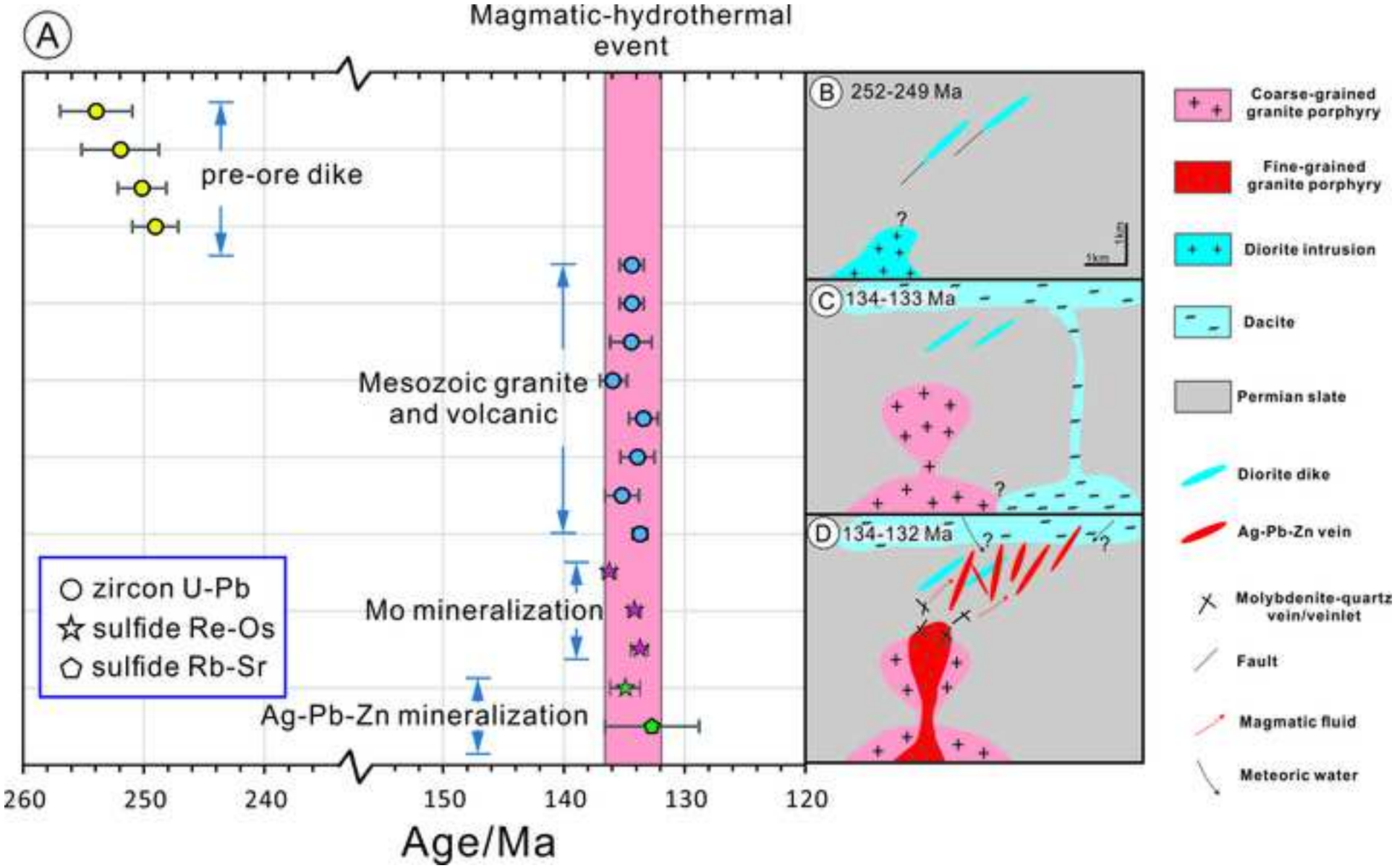

Table 1

Click here to access/download;Table;Table 1 SJ major and trace elements-revised.xlsx

Sample	17SJ-47	17SJ-48	17SJ-59
rock type	granite porphyry (fine-grained)	granite porphyry (fine-grained)	granite porphyry (fine-grained)
wt.%			
SiO_2	80.0	77.3	76.2
TiO_2	0.1	0.1	0.1
Al_2O_3	11.2	12.1	12.9
TFe_2O_3	0.8	1.0	1.1
MnO	0	0	0
MgO	0.2	0.1	0.1
CaO	0.2	0.2	0.6
Na_2O	2.2	3.5	3.7
K_2O	4.6	4.7	4.5
P_2O_5	0	0	0
LOI	0.7	0.7	0.7
ppm			
Sc	1.1	1.1	0.9
Cu	16.3	19.4	23.3
Zn	30.3	31.0	30.3
Ga	17.6	18.6	19.9
Rb	250.8	247.5	252.0
Sr	58.0	54.6	56.1
Y	35.1	31.3	48.4
Zr	101.2	105.7	171.2
Nb	12.6	12.9	14.8
Sn	4.9	5.0	4.5
Cs	9.4	5.9	7.3
Ba	212.7	151.4	152.7
La	21.2	24.4	27.1
Ce	45.7	52.7	57.8
Pr	5.3	6.0	6.7
Nd	18.5	21.3	22.9
Sm	4.1	4.7	5.4
Eu	0.2	0.2	0.2
Gd	3.7	4.2	5.2
Tb	0.7	0.7	1.0
Dy	5.0	4.8	6.7
Ho	1.0	0.9	1.4
Er	3.5	3.0	4.7
Tm	0.6	0.5	0.8
Yb	4.2	3.4	5.5
Lu	0.6	0.5	0.8
Hf	4.3	4.4	6.5
Ta	2.2	2.1	2.4
Pb	36.3	26.2	26.8
Th	32.4	37.3	38.8
U	12.8	19.1	22.3

Table 1 Major and trace element concentrations for magmatic rocks in the Shuangjianzishan ore

17SJ-50	17SJ-51	17SJ-52
granite porphyry (fine-grained)	granite porphyry (coarse-grained)	granite porphyry (coarse-grained)
75.7	69.7	70.0
0.1	0.4	0.4
12.6	14.3	14.4
1.1	2.9	2.9
0	0.1	0.1
0.1	0.6	0.7
0.4	1.6	1.5
3.5	4.1	4.1
4.9	4.3	4.1
0.1	0.1	0.1
0.7	1.4	1.4
1.0	4.4	4.3
3.6	14.8	8.3
27.7	60.1	64.8
20.4	23.0	22.6
276.8	207.4	227.9
55.1	262.0	267.5
34.0	31.9	31.7
125.0	207.8	196.1
15.4	14.0	12.8
3.2	6.0	8.3
8.1	10.4	11.7
150.3	435.7	457.8
25.4	30.2	31.4
54.0	63.9	65.0
6.2	7.4	7.7
21.5	27.5	27.7
4.7	6.2	5.9
0.2	0.7	0.7
4.1	5.3	5.1
0.7	0.9	0.9
4.9	5.5	5.3
1.0	1.0	1.0
3.4	3.2	3.1
0.6	0.5	0.5
4.0	3.3	3.1
0.6	0.5	0.5
5.4	6.9	6.3
2.6	1.5	1.3
26.6	29.9	20.1
39.4	26.0	22.9
15.2	9.0	7.8

district

17SJ-53	17SJ-87	17SJ-24	17SJ-63
granite porphyry (coarse-grained)	granite intrusion (northern part)	granodiorite dike	diorite dike
69.6	73.6	67.3	54.2
0.4	0.2	0.6	0.9
15.3	14.1	16.1	14.7
2.9	1.2	4.3	7.6
0.1	0.0	0.1	0.2
0.7	0.1	1.4	4.7
1.7	0.4	0.4	6.7
4.6	3.3	2.3	3.0
4.0	5.0	4.4	3.5
0.1	0	0.1	0.6
0.9	1.1	2.6	4.1
4.0	3.7	5.6	25.6
4.1	4.1	3.9	39.1
55.9	34.6	1243.9	83.2
23.3	22.7	21.5	16.6
214.2	157.2	122.1	85.9
291.1	21.4	116.3	442.9
33.4	31.0	10.4	22.9
227.1	381.2	225.0	124.0
13.0	13.1	7.9	4.7
11.8	6.0	8.3	2.2
11.4	6.0	14.5	0.5
480.5	145.8	671.6	671.1
24.8	65.9	27.4	12.5
53.5	134.6	54.6	27.6
6.6	15.5	6.2	3.7
24.3	55.4	22.6	15.8
5.5	9.8	4.1	3.8
0.6	0.2	1.0	1.2
5.0	6.9	3.0	3.9
0.8	1.0	0.3	0.6
5.4	6.0	2.0	4.0
1.0	1.1	0.4	0.8
3.3	3.2	1.0	2.4
0.5	0.4	0.1	0.3
3.3	3.1	0.7	2.3
0.5	0.4	0.1	0.4
6.8	10.5	5.4	3.4
1.5	1.0	0.6	0.3
18.1	23.4	261.2	21.6
18.0	22.1	10.6	3.5
6.9	5.3	2.6	1.3

17SJ-60
dacite
65.0
0.6
15.9
4.2
0.1
1.1
1.9
4.6
3.6
0.1
2.2
6.8
5.2
70.0
17.3
74.7
802.9
17.7
196.1
8.1
1.5
2.5
1239.8
31.1
60.6
6.9
24.3
4.3
1.1
3.5
0.5
3.2
0.6
1.8
0.3
1.7
0.3
5.1
0.6
20.6
9.1
2.9

Table 2 In situ sulfur isotope results of ore minerals

Number	Samples	Depth (m)	Ore stage	Minerals	δ^{34}Svcdt (‰)
1	15SJ-16-Q1-Gn-1	230	II-1	Gn	-3.41
2	15SJ-16-Q1-Py-2	230	II-1	Py	-1.11
3	15SJ-16-Q1-Sp-3	230	II-1	Sp	-1.45
4	15SJ-16-Q2-Gn-1	230	II-1	Gn	-4.67
5	15SJ-16-Q2-Sp-2	230	II-1	Sp	-1.53
6	15SJ-16-Q2-Apy-3	230	II-1	Apy	-2.54
7	15SJ-16-Q3-Gn-1	230	II-1	Gn	-3.40
8	15SJ-16-Q3-Gn-2	230	II-1	Gn	-3.51
9	15SJ-16-Q3-Sp-3	230	II-1	Sp	-1.20
10	15SJ-31-Q1-Gn-1	150	II-1	Gn	-3.64
11	15SJ-31-Q1-Gn-2	150	II-1	Gn	-3.48
12	15SJ-31-Q1-Frb-3	150	II-2	Frb	-1.72
13	15SJ-31-Q1-Frb-4	150	II-2	Frb	-1.35
14	15SJ-31-Q4-Frb-1	150	II-2	Frb	-1.18
15	15SJ-31-Q4-Frb-2	150	II-2	Frb	-0.44
16	15SJ-43-Q1-Gn-1	190	II-1	Gn	-3.79
17	15SJ-43-Q1-Gn-2	190	II-1	Gn	-3.53
18	15SJ-43-Q1-Gn-3	190	II-1	Gn	-3.35
19	15SJ-43-Q1-Gn-4	190	II-1	Gn	-3.66
20	15SJ-43-Q1-Gn-5	190	II-1	Gn	-3.22
21	15SJ-43-Q2-Gn-1	190	II-1	Gn	-4.62
22	15SJ-43-Q2-Gn-2	190	II-1	Gn	-3.83
23	15SJ-43-Q2-Py-3	190	I	Py	-1.65
24	15SJ-43-Q2-Sp-4	190	II-1	Sp	-1.07
25	15SJ-51-Q1-Gn-1	230	II-1	Gn	-3.14
26	15SJ-51-Q1-Gn-2	230	II-1	Gn	-3.11
27	15SJ-51-Q1-Gn-3	230	II-1	Gn	-4.51
28	15SJ-51-Q1-Sp-4	230	II-1	Sp	-0.79
29	15SJ-51-Q1-Sp-5	230	II-1	Sp	-2.39
30	15SJ-51-Q2-Gn-1	230	II-1	Gn	-3.42
31	15SJ-51-Q2-Gn-2	230	II-1	Gn	-4.10
32	15SJ-51-Q2-Sp-3	230	II-1	Sp	-1.21
33	15SJ-51-Q2-Sp-4	230	II-1	Sp	-2.76
34	15SJ-84-Q1-Gn-1	110	II-1	Gn	-3.68
35	15SJ-84-Q1-Py-2	110	II-1	Py	-0.87
36	15SJ-84-Q1-Sp-3	110	II-1	Sp	-0.62
37	15SJ-84-Q2-Gn-1	110	II-1	Gn	-3.78
38	15SJ-84-Q2-Gn-2	110	II-1	Gn	-3.96
39	15SJ-84-Q2-Py-3	110	II-1	Py	-1.27

Abbreviations: Apy-asenopyrite; Caf-canfieldite; Ccp-chalcopyrite; Frb-freibergite; Gn-galena; Py-pyrite; Py

in the Shuangjianishan Ag-Pb-Zn deposit

Number	Samples	Depth (m)	Ore stage	Minerals	δ^{34}Svcdt (‰)
40	15SJ-84-Q3-Apy-1	110	II-1	Apy	-1.36
41	15SJ-84-Q4-Apy-1	110	II-1	Apy	-1.08
42	15SJ-94-Q1-Pyr-1	110	II-2	Pyr	2.13
43	15SJ-94-Q1-Pyr-2	110	II-2	Pyr	2.44
44	15SJ-94-Q1-Pyr-3	110	II-2	Pyr	1.41
45	15SJ-94-Q1-Caf-4	110	II-2	Caf	-0.65
46	15SJ-94-Q1-Gn-5	110	II-1	Gn	-3.85
47	15SJ-94-Q2-Gn-1	110	II-1	Gn	-3.47
48	15SJ-94-Q2-Caf-2	110	II-2	Caf	-1.94
49	15SJ-94-Q2-Ccp-3	110	II-1	Ccp	-1.86
50	15SJ-94-Q3-Caf-1	110	II-2	Caf	-1.35
51	15SJ-94-Q4-Caf-1	110	II-2	Caf	-1.87
52	15SJ-94-Q4-Caf-2	110	II-2	Caf	-1.91
53	15SJ-94-Q5-Caf-1	110	II-2	Caf	-1.53
54	15SJ-94-Q5-Sp-2	110	II-1	Sp	0.27
55	15SJ-94-Q5-Py-3	110	II-1	Py	-1.80
56	15SJ-94-Q5-Gn-4	110	II-1	Gn	-3.25
57	15SJ-97-Q1-Py-1	110	I	Py	-1.27
58	15SJ-97-Q1-Py-2	110	I	Py	-1.19
59	15SJ-97-Q1-Ccp-3	110	II-1	Ccp	-1.42
60	15SJ-97-Q1-Ccp-4	110	II-1	Ccp	-1.71
61	15SJ-97-Q1-Sp-5	110	II-1	Sp	-1.17
62	15SJ-97-Q2-Ccp-1	110	II-1	Ccp	-1.13
63	15SJ-97-Q2-Gn-2	110	II-1	Gn	-1.54
64	15SJ-97-Q2-Py-3	110	I	Py	-1.22
65	15SJ-97-Q2-Sp-4	110	II-1	Sp	-0.88
66	15SJ-99-Q1-Apy-1	110	II-1	Apy	-0.39
67	15SJ-99-Q1-Sp-2	110	II-1	Sp	-0.91
68	15SJ-99-Q1-Gn-3	110	II-1	Gn	-3.49
69	15SJ-99-Q1-Ccp-4	110	II-1	Ccp	-1.78
70	15SJ-99-Q2-Gn-1	110	II-1	Gn	-2.74
71	15SJ-99-Q2-Gn-2	110	II-1	Gn	-2.57
72	15SJ-104-Q1-Py-1	190-210	II-1	Py	-0.92
73	15SJ-104-Q1-Sp-2	190-210	II-1	Sp	-2.47
74	15SJ-104-Q1-Gn-3	190-210	II-1	Gn	-4.57
75	15SJ-104-Q2-Sp-1	190-210	II-1	Sp	-2.95
76	15SJ-104-Q2-Gn-2	190-210	II-1	Gn	-4.18
77	15SJ-104-Q2-Py-3	190-210	I	Py	-1.36

r-pyrargyrite; Sp-sphalerite.

Table 3

Click here to access/download;Table;Table 3 SJ lead isotope results.xlsx

Table 3 In situ lead isotope results of ore minerals in the Shuangji

Number	Samples	Depth (m)	Ore stage	Minerals	$^{206}Pb/^{204}Pb$
1	15SJ-104-q1-py-1	190-210	I	Pyrite	18.308
2	15SJ-104-q1-sp-1	190-210	II-1	Sphalerite	18.264
3	15SJ-104-q1-apy-1	190-210	II-1	Arsenopyrite	18.279
4	15SJ-104-q2-gn-3	190-210	II-1	Galena	18.283
5	15SJ-104-q2-py-1	190-210	II-1	Pyrite	18.284
6	15SJ-104-q2-sp-1	190-210	II-1	Sphalerite	18.244
7	15SJ-16-q1-gn-1	230	II-1	Galena	18.282
8	15SJ-16-q1-py-1	230	II-1	Pyrite	18.269
9	15SJ-16-q1-sp-1	230	II-1	Sphalerite	18.303
10	15SJ-16-q2-gn-1	230	II-1	Galena	18.283
11	15SJ-16-q2-sp-1	230	II-1	Sphalerite	18.279
12	15SJ-16-q2-apy-1	230	II-1	Arsenopyrite	18.281
13	15SJ-16-q3-gn-1	230	II-1	Galena	18.283
14	15SJ-16-q3-gn-2	230	II-1	Galena	18.281
15	15SJ-16-q3-sp-1	230	II-1	Sphalerite	18.275
16	15SJ-31-q1-frb-1	150	II-2	Freibergite	18.280
17	15SJ-31-q4-gn-1	150	II-1	Galena	18.285
18	15SJ-31-q4-gn-2	150	II-1	Galena	18.284
19	15SJ-43-q1-gn-1	190	II-1	Galena	18.277
20	15SJ-43-q1-gn-2	190	II-1	Galena	18.277
21	15SJ-43-q1-gn-3	190	II-1	Galena	18.276
22	15SJ-43-q1-gn-4	190	II-1	Galena	18.285
23	15SJ-43-q1-gn-5	190	II-1	Galena	18.286
24	15SJ-43-q2-gn-1	190	II-1	Galena	18.274
25	15SJ-43-q2-gn-2	190	II-1	Galena	18.278
26	15SJ-43-q2-py-1	190	II-1	Pyrite	18.290
27	15SJ-43-q2-sp-1	190	II-1	Sphalerite	18.274
28	15SJ-51-q1-gn-1	230	II-1	Galena	18.286
29	15SJ-51-q1-gn-2	230	II-1	Galena	18.285
30	15SJ-51-q1-gn-3	230	II-1	Galena	18.282
31	15SJ-51-q1-sp-1	230	II-1	Sphalerite	18.282
32	15SJ-51-q1-sp-2	230	II-1	Sphalerite	18.271
33	15SJ-51-q2-gn-1	230	II-1	Galena	18.282
34	15SJ-51-q2-gn-2	230	II-1	Galena	18.283
35	15SJ-51-q2-sp-1	230	II-1	Sphalerite	18.282
36	15SJ-51-q2-sp-2	230	II-1	Sphalerite	18.243
37	15SJ-84-q1-gn-1	110	II-1	Galena	18.284
38	15SJ-84-q1-py-1	110	I	Pyrite	18.310
39	15SJ-84-q2-gn-1	110	II-1	Galena	18.286
40	15SJ-84-q2-gn-2	110	II-1	Galena	18.285
41	15SJ-84-q2-py-1	110	I	Pyrite	18.288
42	15SJ-84-q3-apy-1	110	II-1	Arsenopyrite	18.266
43	15SJ-84-q4-apy-1	110	II-1	Arsenopyrite	18.283
44	15SJ-94-q1-gn-1	110	II-1	Galena	18.283
45	15SJ-94-q2-gn-1	110	II-1	Galena	18.283
46	15SJ-97-q1-ccp-1	110	II-1	Chalcopyrite	18.273
47	15SJ-97-q1-ccp-2	110	II-1	Chalcopyrite	18.274
48	15SJ-97-q1-py-1	110	I	Pyrite	18.268
49	15SJ-97-q1-py-2	110	I	Pyrite	18.259

50	15SJ-97-q1-sp-1	110	II-1	Sphalerite	18.277
51	15SJ-97-q2-ccp-1	110	II-1	Chalcopyrite	18.283
52	15SJ-97-q2-gn-1	110	II-1	Galena	18.279
53	15SJ-97-q2-py-1	110	I	Pyrite	18.275
54	15SJ-97-q2-sp-1	110	II-1	Sphalerite	18.279
55	15SJ-99-q1-gn-1	110	II-1	Galena	18.279
56	15SJ-99-q1-py-1	110	I	Pyrite	18.278
57	15SJ-99-q1-sp-1	110	II-1	Sphalerite	18.275
58	15SJ-99-q2-gn-1	110	II-1	Galena	18.278
59	15SJ-99-q2-gn-1	110	II-1	Galena	18.281

ianzishan Ag-Pb-Zn deposit

1σ	$^{207}Pb/^{204}Pb$	1σ	$^{208}Pb/^{204}Pb$	1σ
0.020	15.561	0.018	38.203	0.042
0.026	15.521	0.023	38.105	0.056
0.003	15.535	0.003	38.142	0.009
0.002	15.542	0.002	38.163	0.006
0.006	15.540	0.005	38.155	0.013
0.015	15.509	0.013	38.073	0.031
0.002	15.540	0.002	38.148	0.006
0.009	15.522	0.008	38.062	0.022
0.004	15.560	0.004	38.194	0.012
0.002	15.539	0.002	38.146	0.005
0.006	15.533	0.005	38.128	0.015
0.004	15.533	0.004	38.123	0.010
0.002	15.540	0.002	38.150	0.006
0.002	15.537	0.002	38.142	0.007
0.013	15.515	0.012	38.116	0.029
0.010	15.549	0.010	38.166	0.032
0.002	15.542	0.002	38.158	0.007
0.002	15.542	0.002	38.156	0.007
0.002	15.537	0.002	38.151	0.006
0.002	15.538	0.002	38.152	0.006
0.003	15.537	0.003	38.148	0.008
0.002	15.542	0.002	38.159	0.006
0.002	15.543	0.002	38.157	0.006
0.002	15.536	0.002	38.144	0.007
0.002	15.538	0.003	38.152	0.007
0.004	15.543	0.004	38.159	0.011
0.007	15.526	0.006	38.096	0.017
0.002	15.544	0.002	38.164	0.007
0.002	15.542	0.002	38.157	0.005
0.002	15.540	0.002	38.153	0.006
0.026	15.543	0.022	38.169	0.055
0.005	15.530	0.005	38.127	0.013
0.002	15.538	0.002	38.146	0.006
0.002	15.540	0.002	38.151	0.005
0.002	15.540	0.002	38.154	0.006
0.015	15.503	0.013	38.053	0.032
0.002	15.543	0.002	38.163	0.006
0.016	15.563	0.014	38.197	0.035
0.002	15.542	0.002	38.156	0.006
0.003	15.543	0.003	38.161	0.008
0.005	15.545	0.005	38.167	0.012
0.004	15.522	0.003	38.103	0.010
0.002	15.539	0.002	38.147	0.007
0.003	15.542	0.003	38.164	0.008
0.002	15.542	0.002	38.159	0.006
0.006	15.529	0.006	38.128	0.020
0.006	15.531	0.006	38.127	0.015
0.004	15.526	0.004	38.114	0.011
0.010	15.512	0.009	38.061	0.023

0.004	15.531	0.004	38.123	0.010
0.008	15.537	0.007	38.142	0.020
0.002	15.539	0.002	38.154	0.007
0.002	15.532	0.003	38.136	0.008
0.006	15.536	0.006	38.146	0.016
0.003	15.540	0.003	38.160	0.008
0.001	15.538	0.002	38.150	0.005
0.007	15.539	0.006	38.140	0.016
0.002	15.538	0.002	38.150	0.007
0.002	15.541	0.003	38.162	0.007

Table 4 Molybdenite Re-Os results of the Shuangjianzishan Ag-Pb

Sample	wt (g)	Re (ppm)	±2σ	^{187}Re (ppm)	±2σ	^{187}Os (ppb)	±2σ
17SJ-34	0.021	2.640	0.012	1.659	0.008	3.773	0.015
17SJ-35	0.061	0.119	0.001	0.075	0.001	0.167	0.001
17SJ-41	0.059	1.994	0.008	1.253	0.005	2.805	0.009

[a]uncertainty including only mass spectrometry uncertainty

[b]uncertainty including all sources of analytical uncertainty

[c]uncertainty including all sources of analytical uncertainty plus decay constant

-Zn deposit

Age (Ma)	±2σ[a]	±2σ[b]	±2σ[c]
136.31	0.15	0.75	0.87
133.69	0.01	1.13	1.20
134.19	0.12	0.66	0.78

Table 5

Table 5 Pyrite Re-Os

Samples	Re (ppb)	±2σ	^{187}Re (ppb)	±2σ	Total Os (ppt)	±2σ	^{192}Os (ppt)	±2σ	$^{187}Os^{r}$ (ppt)
15SJ-10	0.262	0.001	0.164	0.001	2.198	0.069	0.670	0.041	0.371
15SJ-16	0.520	0.003	0.327	0.002	1.446	0.782	0.164	0.085	0.736
17SJ-26	0.886	0.003	0.557	0.002	13.082	0.153	3.546	0.065	1.253
15SJ-114	1.077	0.004	0.677	0.002	1.483	1.252	0.061	0.040	1.317

Note: The initial $^{187}Os/^{188}Os$ (Os_i) values, with the exception of sample 15SJ-114, are assumed to have a large range fro

data of the Shuangjianzishan Ag-Pb-Zn deposit

±2σ	$^{187}Os^{r}$ %	$^{187}Re/^{188}Os$	±2σ	$^{187}Os/^{188}Os$	±2σ	rho	% Re blank	% ^{187}Os blank
0.028	60.7	776.4	48.0	2.8	0.2	0.98	2.2	0.9
0.170	69.3	6309.3	3269.9	20.4	10.6	1.00	2.3	1.1
0.146	27.0	496.9	9.2	4.1	0.1	0.78	0.6	0.1
0.041	99.3	34959.9	23095.1	69.0	45.6	1.00	0.5	0.4

ɔm ~1.1 to 6.2; uncertainty correlation factor (rho) is applied to assess the degree of correlation between $^{187}Re/$

% ^{188}Os blank	Os_i (ppt)	Age (Ma)
10.9	1.09	134.5
50.8	6.16	135.6
2.2	3.02	135.0
56.9	-	118.1

/^{188}Os and ^{187}Os/^{188}Os ratios.

Figure A1

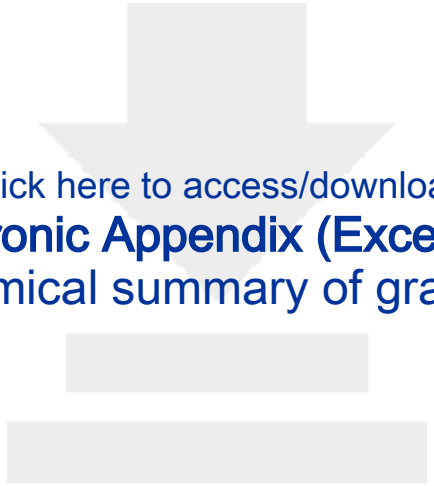

Click here to access/download

Electronic Appendix (Excel etc.)

Fig A1 Petrochemical summary of granites revised.jpg

Figure A2

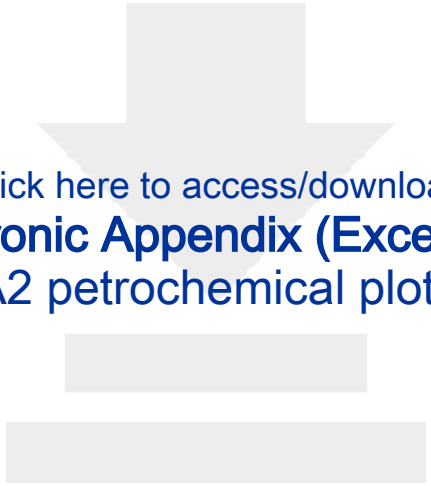

Click here to access/download

Electronic Appendix (Excel etc.)

Fig A2 petrochemical plots.jpg

Figure A3

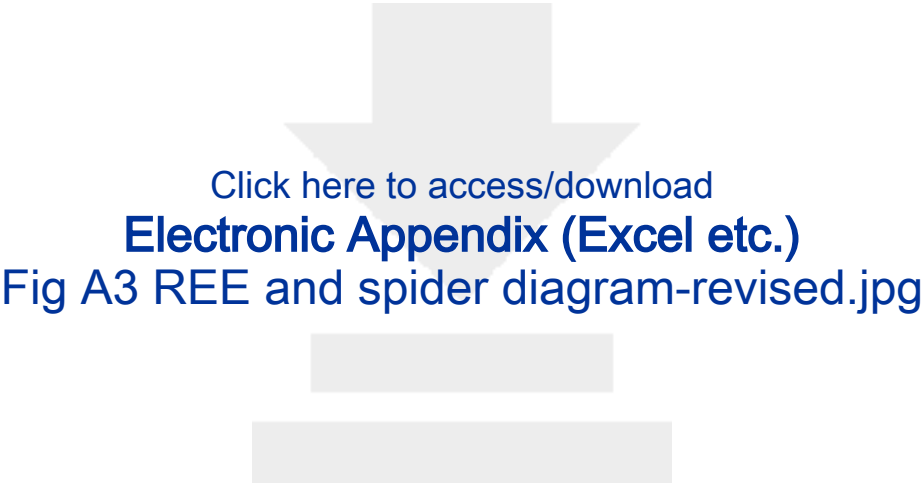

Click here to access/download

Electronic Appendix (Excel etc.)

Fig A3 REE and spider diagram-revised.jpg

Figure A4

Click here to access/download

Electronic Appendix (Excel etc.)

Fig A4 Hisgram T of S isotope.jpg

Figure A5

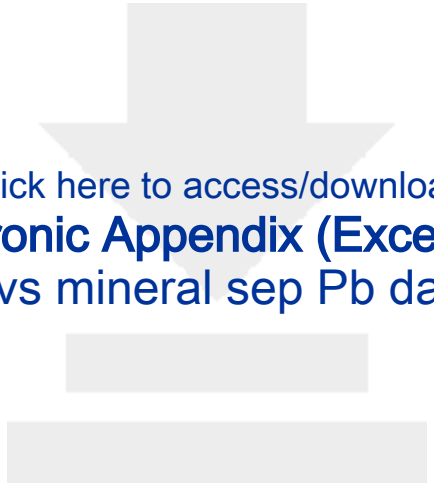

Click here to access/download

Electronic Appendix (Excel etc.)

Fig A5 in situ vs mineral sep Pb data-revised.jpg

Figure A6

Click here to access/download

Electronic Appendix (Excel etc.)

Fig A6 trace element diagram.jpg

Table A1

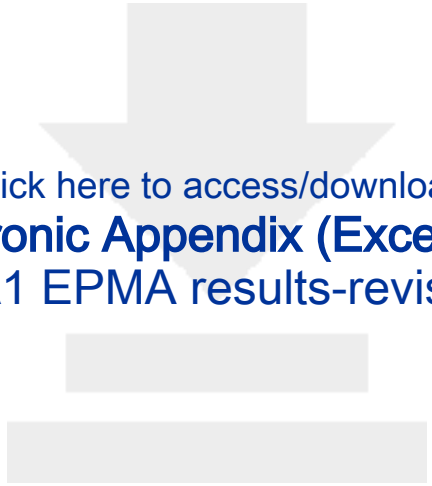

Click here to access/download

Electronic Appendix (Excel etc.)

Table A1 EPMA results-revised.xlsx

Table A2

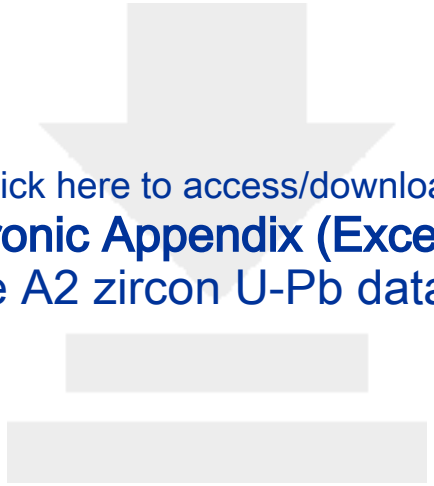

Click here to access/download

Electronic Appendix (Excel etc.)

Table A2 zircon U-Pb data.xlsx

Table A3